

# Iterative thermodynamic modelling—Part 1: A theoretical scoring technique and a computer program (BINGO-ANTIDOTE)

Erik Duesterhoeft<sup>1</sup>  | Pierre Lanari<sup>2</sup> 

<sup>1</sup>Institute of Geosciences, CAU University Kiel, Kiel, Germany

<sup>2</sup>Institute of Geological Sciences, University of Bern, Bern, Switzerland

## Correspondence

Erik Duesterhoeft, Institute of Geosciences, CAU University Kiel, Kiel, Germany.

Email: erik.dueterhoeft@ifg.uni-kiel.de

## Funding information

Deutsche Forschungsgemeinschaft, Grant/Award Number: DU1603/1-1

## Abstract

This paper introduces the software solution BINGO-ANTIDOTE for thermodynamic calculations at equilibrium based on iterative thermodynamic models. It describes a hybrid strategy combining the strength of Gibbs energy minimization (GEM) and inverse thermobarometry models based on the comparison between the modelled and observed mineral assemblage, modes and compositions. The overall technique relies on quantitative compositional maps acquired by electron probe micro-analyser for obtaining a mutually consistent set of observed data such as bulk rock and mineral compositions. Thus it offers the opportunity to investigate metamorphic rocks on a microscale. The scoring part BINGO integrates three statistical model quality factors  $Q_{asm}$  for the assemblage,  $Q_{vol}$  for the mineral modes,  $Q_{cmp}$  for the mineral compositions combined in a global evaluation criterion  $Q_{total}$  that quantifies how the model reproduces the observations for the investigated volume. The input parameters of GEM affecting the model quality such as pressure, temperature and eventually some components of the bulk composition (e.g. the molar amount of hydrogen, carbon or oxygen) or activity variables of fluids and gases (e.g.  $a_{H_2O}$ ,  $a_{CO_2}$ ,  $f(O_2)$ ) can be optimized by inversion in ANTIDOTE using several mapping stages followed by a direct search optimization. Examples of iterative models based on compositional maps processed with BINGO-ANTIDOTE demonstrate the utility of the program. In contrast to the qualitative interpretation of phase diagrams, the inversion maximizes the benefits of GEM and permits the derivation of statistically ‘optimal’ pressure–temperature conditions for well-equilibrated samples. In addition, BINGO-ANTIDOTE opens new avenues for petrological investigations such as the generation of chemical potential landscape maps.

## KEYWORDS

BINGO-ANTIDOTE, compositional mapping, inversion, model evaluation, phase equilibria

This is an open access article under the terms of the Creative Commons Attribution-NonCommercial-NoDerivs License, which permits use and distribution in any medium, provided the original work is properly cited, the use is non-commercial and no modifications or adaptations are made.

© 2020 The Authors. *Journal of Metamorphic Geology* published by John Wiley & Sons Ltd.

# 1 | INTRODUCTION

The quantitative investigation of metamorphic rocks often requires the application of petrological models based on the concept of equilibrium thermodynamics. With the rise of personal computers in science in the mid-1980s, a large variety of petrological programs and software solutions were developed (see Lanari & Duesterhoeft, 2019; Spear, Pattison, & Cheney, 2016 for review). Their applications have significantly enhanced our knowledge of the metamorphic conditions reached in the Earth's crust, but also offered modelling strategies to better understand key metamorphic processes (e.g. Yakymchuk, 2017).

One efficient way to forward model the consequences of a metamorphic transformation at constant pressure ( $P$ ), temperature ( $T$ ) and bulk composition ( $X$ ) is to apply Gibbs energy minimization (GEM) to a closed system (Brown & Skinner, 1974; Connolly & Kerrick, 1987; de Capitani & Brown, 1987). This computation reproduces the behaviour of natural metamorphic systems, which are supposed to converge towards a stable state of internal energy known as thermodynamic equilibrium.

The apparent low number of assumptions required for applying GEM to natural mineral assemblages is probably the main reason for the popularity of this technique. The knowledge of the bulk rock composition is usually sufficient to generate a phase diagram with THERIAK-DOMINO (de Capitani & Brown, 1987; de Capitani & Petrakakis, 2010), PERPLE\_X (Connolly, 1990, 2005, Connolly 2009) or THERMOCALC (Powell & Holland, 2008; Powell, Holland, & Worley, 1998) and to identify at which conditions the inferred mineral assemblage is predicted to be stable. But are these conditions representative of a palaeo-equilibrium state reached by the sample? The answer is probably yes if the following conditions are met:

1. All the minerals grew or were re-equilibrated at the same time.
2. Local chemical equilibrium was achieved to a satisfactory degree via the intergranular medium for the elements of interest.
3. The mineral compositions were not modified during subsequent heating/cooling or by fluid-mediated alteration.

Those assumptions are often hard to test in nature. Metamorphic rocks commonly exhibit a high degree of complexity with mineral relics and compositional zoning. The application of an equilibrium model can be biased due to the effect of compositional heterogeneities associated with sluggish diffusion (e.g. Guevara & Caddick, 2016; Lanari & Engi, 2017; Palin, Weller, Waters, & Dyck, 2016; Stüwe, 1997; Tajčmanová, Konopásek, & Schulmann, 2006) or if kinetic factors played a significant role (e.g. Carlson,

## Highlights

- Hybrid modelling strategy for thermobarometry.
- Description of the software solution BINGO-ANTIDOTE.
- Determination of metamorphic conditions from compositional maps.
- Estimation of relative uncertainties.

Pattison, & Caddick, 2015; Pattison & Spear, 2018; Waters & Lovegrove, 2002). Despite several recent efforts (e.g. Green et al., 2016; Shrestha, Larson, Duesterhoeft, Soret, & Cottle, 2019; Spear & Pyle, 2010; White, Powell, Holland, Johnson, & Green, 2014), the overall quality of the thermodynamic databases remains a challenge when reproducing natural samples. If the conditions listed above are not fulfilled, deviations are expected to occur between the model and the behaviour of natural system.

One of the existing limitations of the GEM technique largely lies in the absence of a statistical framework to quantify the degree of matching between the results of GEM and the observations for a specific sample (natural or experimental). As a consequence, the model outcomes are never fully compared with the rock record (Figure 1) and the comparison is rather restricted to the mineral assemblage with sometimes the addition of a few diagnostic isopleths (Lanari & Duesterhoeft, 2019; Powell & Holland, 2008). The goal of this paper is to bridge this gap by providing a mutually consistent framework for the application of GEM to local mineral assemblages in which the local bulk composition and the observations (mineral assemblage, modes and compositions) are determined from the same volume of rock. This framework includes a scoring technique that quantitatively compares the model results with the observations and an automated optimization routine for the inversion. The computations are performed using the open-source program BINGO-ANTIDOTE available at <https://www.xmaptools.com/bingo-antidote/> and integrated in the module XTHERMOTOOLS which can readily handle quantitative compositional maps generated by XMAPTOOLS (Lanari, Vho, Bovay, Airaghi, & Centrella, 2019; Lanari et al., 2014).

## 1.1 | The concept of iterative thermodynamic models

The thermodynamic models used in petrology are either designed to solve forward or inverse problems. *Forward models* calculate what should be observed in metamorphic systems, that is, they simulate metamorphism at equilibrium conditions and compute mineral assemblage, modes and compositions

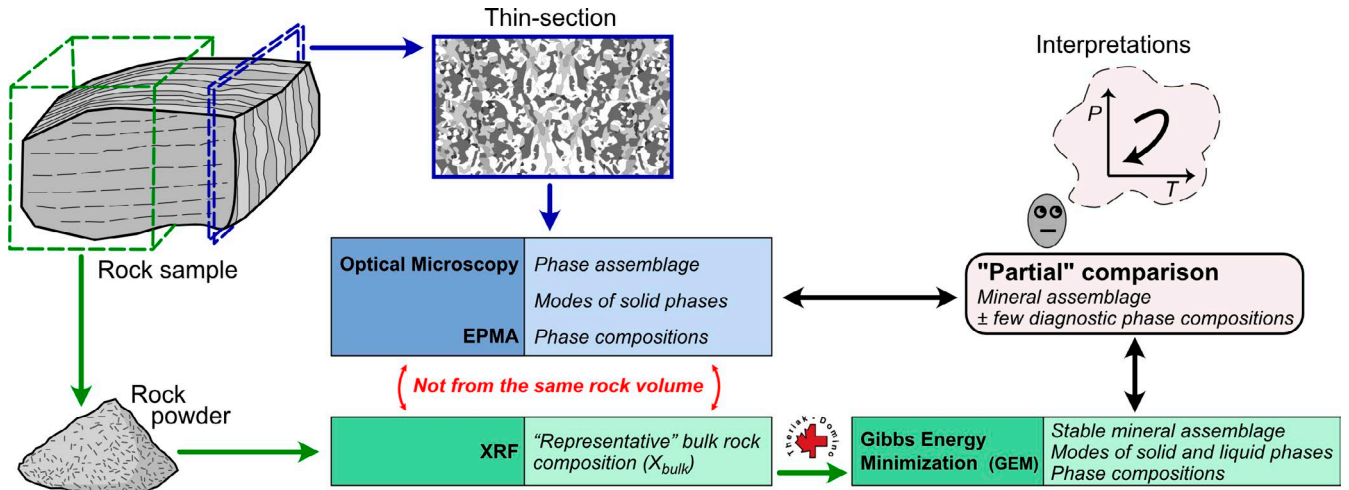


**FIGURE 1** Classical sample preparation and analytical strategy for thermobarometry. This strategy commonly involves the analysis of two separate pieces of a single sample. The bulk composition ( $X_{\text{bulk}}$ ) used in GEM-based models is obtained by XRF from rock powder. The observations (mineral assemblage, modes and compositions) are obtained from the analysis made on a thin section of rock. As the observations and models are derived from two separate pieces of samples (green and blue paths), they can only be partially and qualitatively compared

from the causal factors that produced them—essentially  $P$ ,  $T$  and  $X_{\text{bulk}}$  and, in externally buffered system, the chemical potential. *Inverse models* start with the results—the mineral compositions—and then calculate the causes—mainly  $P$  and  $T$ . Both strategies have limitations that are listed and discussed in the recent paper of Lanari and Dueterhoeft (2019).

We define *iterative thermodynamic models* as hybrid models built on a forward simulation (namely GEM) and then coupled to an iterative optimization refining the causal factors (Figure 2b). Such model requires a statistical framework comparing model outcomes and observations. An example of simple iterative model is presented in Lanari, Giuntoli, Loury, Burn, and Engi (2017). In this case, the misfit factor used in

the optimization of  $P$ - $T$ - $X_{\text{bulk}}$  is based on the comparison between the modelled and observed compositions of successive growth zones of garnet. A generalized iterative model (not only applicable to garnet) is presented in this study.

### 1.2 | A mutually consistent strategy based on quantitative compositional mapping

*Classical sample preparation and analytical strategy* of petrological studies generally require two separate pieces of a single sample (Figure 1). The first (~1 kg) is crushed and powdered in a shatterbox. The powder is analysed

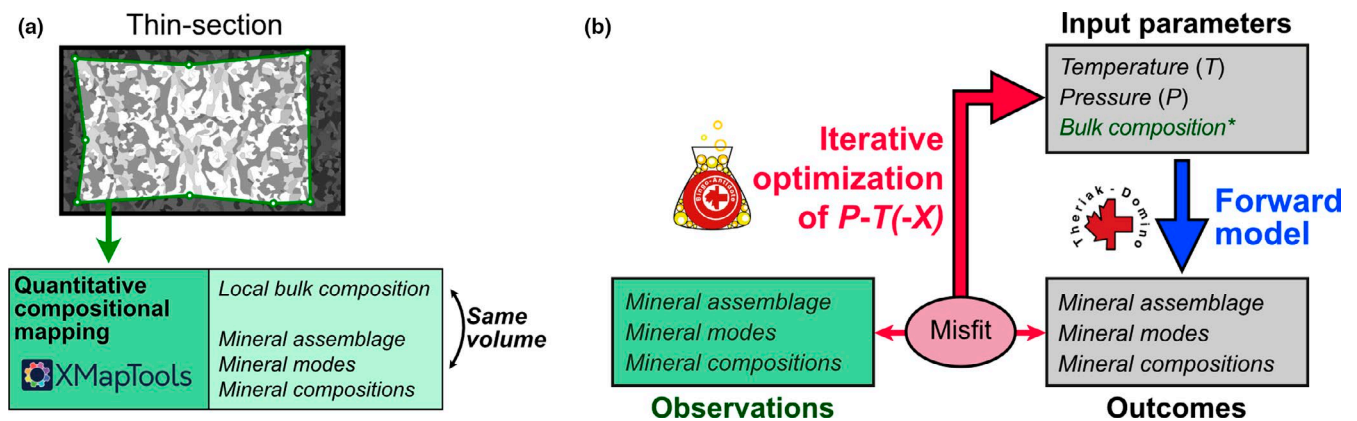


**FIGURE 2** Iterative Thermodynamic Modelling (ITM) strategy based on compositional maps. (a) An area-of-interest is defined and combined with quantitative compositional maps for extracting a local bulk composition (LEB) along with the observations (mineral assemblage, modes and compositions). (b) Iterative thermodynamic modelling combining a forward model (blue arrow) and an iterative inversion (red arrow). The misfit parameter can either be  $Q_{\text{total1}}$  or  $Q_{\text{total2}}$  (see text). Abbreviations:  $X$  indicates some components of the bulk composition (e.g. the molar amount of hydrogen, carbon or oxygen) or activity variables of fluids and gases (e.g.  $a_{\text{H}_2\text{O}}$ ,  $a_{\text{CO}_2}$ ,  $f(\text{O}_2)$ ). \*Note that the local bulk composition determined in (a) is taken as bulk composition in (b). In this case, the observations and model are derived from the same volume

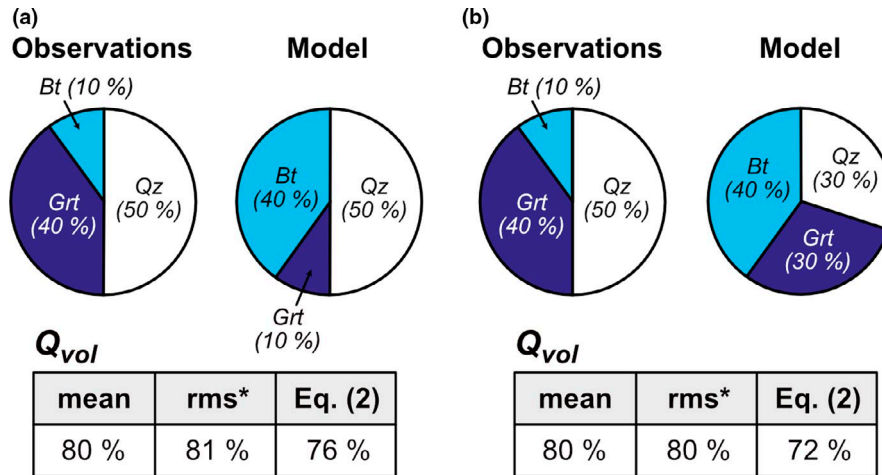


**FIGURE 3** Theoretical examples comparing the evaluation criterion  $Q_{vol}$  defined in Equation 2 (label: ‘Equation 2’) with simple functions such as arithmetic mean (label: ‘mean’) or root mean square (label: ‘rms\*’). The arithmetic mean of examples (a) and (b) are identical whereas (a) must be higher ranked because the modelled minerals modes would be identically with the observation by swapping garnet and biotite. Such discrepancies can be attributed to limitations in the thermodynamic models (e.g. incorrect standard state properties or activity models) of the affected mineral phases and introduces a systematic error. By contrast, the case in (b) shows a poor match that is not attributed to such systematic errors

for major element concentration via X-ray fluorescence (XRF) resulting in a measurement of the ‘representative’ bulk rock composition ( $X_{bulk}$ ). The mineral observations are made on the second piece mounted on a glass plate and finely polished until obtaining a thin section (Figure 1). In most cases, Electron Probe Micro-Analysis (EPMA) is used to determine the chemistry of mineral phases. As a consequence, the outcomes of the model controlled by  $X_{bulk}$  (via the mass-balance equation in GEM) cannot be fully compared from a statistical point of view with the observations from thin section that correspond to another volume of the rock sample (Figure 1). Only a rough comparison is possible, provided that the thin section is representative of the rock volume modelled.

An alternative strategy uses semi-quantitative compositional maps obtained by EPMA on the polished thin section and transforms them to maps of oxide weight percentage composition (Clarke, Daczko, & Nockolds, 2001; De Andrade, Vidal, Lewin, O’Brien, & Agard, 2006). Hence, a local bulk composition (LBC) can be calculated from an area-of-interest within the mapped area by integrating the pixel compositions, and the corresponding mineral modes and compositions are available (Figure 2a). Iterative models based on such data set are mutually consistent because the outcomes constrained by  $X_{bulk}$  and the observations are derived from the same surface of rock and extrapolated to the volume to be modelled. Guidelines for selecting the domain are given in Lanari and Engi (2017) and Lanari and Duesterhoeft (2019). This aspect will be the main focus of the second paper of this series. In the following we introduce BINGO-ANTIDOTE that is built upon the THERIAK-DOMINO software package.

## 2 | BINGO—A SCORING TECHNIQUE FOR COMPARING THE RESULTS OF GEM WITH OBSERVATIONS

The scoring technique presented in the following aims to evaluate the overall quality of GEM results based on LBCs obtained from quantitative compositional maps. The *model quality factors* ( $Q$ ) quantify how well the model outcomes reproduces (or not) the corresponding observations for the investigated volume, assuming that the minerals formed in equilibrium and their compositions were preserved upon exhumation and cooling (see conditions 1–3 above). This flexible model scorer is based on three independent evaluation criteria for the assemblage ( $Q_{asm}$ ), the mineral modes ( $Q_{vol}$ ) and the mineral compositions ( $Q_{cmp}$ ), plus one dependent global evaluation criterion ( $Q_{total}$ ). These criteria are described in the following and a case study is presented to illustrate the strategy. This scoring technique is implemented in the program BINGO that evaluates  $Q_{asm}$ ,  $Q_{vol}$ ,  $Q_{cmp}$  and  $Q_{total}$  for any set of  $P$ – $T$ – $X_{bulk}$  conditions.

### 2.1 | Mineral assemblage

The first *model quality factor*  $Q_{asm}$  is determined by statistical analysis, involving the comparison of the modelled assemblage, composed by  $m$  phases  $P_{i=1:m}^{mod}$  with the observed assemblage composed by  $n$  phases  $P_{i=1:n}^{obs}$ . If model and observations are identical,  $Q_{asm}$  is of 100% (likelihood of 1). If

**TABLE 1** Selected elements for comparison between observed and modelled mineral compositions used in this study

	Si	Ti	Al	Fe	Mn	Mg	Ca	Na	K
Biotite	x	x	x	x		x			
Garnet				x	x	x	x		
Plagioclase	x		x				x	x	x
Staurolite						x			
Quartz	x								
Sillimanite			x						

at least one phase is not listed either in the model or in the observed assemblage,  $Q_{asm}$  is estimated as:

$$Q_{asm} = 100 \times \frac{1}{k} \quad (1)$$

with  $l$  the number of matching phases between  $P_{i=1:m}^{mod}$  and  $P_{i=1:n}^{obs}$  and  $k$  the total number of different phases involved in model and observations.

## 2.2 | Mineral modes

The second *model quality factor*  $Q_{vol}$  evaluates the degree of matching between modelled and observed mineral modes using the volume fractions ( $v_i$ ). The mineral surface fractions in the classified map are assumed to be equivalent to the volume fractions ( $v_i$ ) of each mineral phase in the selected area, as for calculating the local bulk composition (see appendix 1 in Lanari & Engi, 2017). The following relationship is used for evaluating  $Q_{vol}$  from the  $l$  matching phases:

$$Q_{vol} = 100 \cdot \sqrt{\sum_{i=1}^l \frac{(v_i^{mod} + v_i^{obs})}{2} \cdot \left[ 1 - \frac{abs(v_i^{mod} - v_i^{obs})}{(v_i^{mod} + v_i^{obs})} \right]^2} \quad (2)$$

with  $v_i^{mod}$  and  $v_i^{obs}$  respectively the model and observed volume fractions of phase  $i$ . A weighted root mean square approach is applied instead of a simple root mean square approach because the mineral modes of a given assemblage are not independent of each other due to competitive element partitioning (see Figure 3). Figure 3 shows that the arithmetic mean (mean) or simple root mean square (rms) approaches are not sensitive to such interdependencies (compare Figure 3a,b) and result in the same  $Q_{vol}$  value as for a 'truly' low correlation between model and observed volume fractions. The first factor of Equation 2 under the root symbol (mean square) is unweighted, whereas the second factor weights the minerals with higher modes stronger than those with lower modes. Such a weighting procedure is required for obtaining a robust evaluation of  $Q_{vol}$  as the modal estimation of small minerals (<1 vol.%) usually holds higher uncertainties for compositional maps having a low spatial

resolution. Possible underestimation of the surface fraction of small phases and the corresponding underestimation of  $Q_{vol}$  is minimized. In addition, the weighting buffers systematic deviations caused by inaccurate thermodynamic data (standard state properties or activity models) that affect the mineral compositions and therefore the mineral modes for maintaining mass balance (see Equation 2 and Figure 3). The second factor under the root symbol is the normalized degree of fit between modelled and observed mineral modes. It is important to note that this model quality factor is calculated only for the matching phases in order to keep it independent from  $Q_{asm}$ . Consequently, it is not possible to calculate  $Q_{vol}$  in the absence of matching phases (if  $Q_{asm} = 0\%$ ).

## 2.3 | Mineral compositions

The third *model quality factor*  $Q_{cmp}$  evaluates the quality of the modelled mineral compositions by comparing with the observed compositions. This comparison is based on the chemical composition of each phase expressed in number of atoms per formula unit (apfu) and normalized to the same number of oxygen. Several successive steps are necessary to evaluate the final  $Q_{cmp}$  from the composition of the matching phases.

For a given phase  $i$  present in the model and in the observations, the absolute difference in composition of element  $j$  is obtained by:

$$\Delta_{i,j} = abs \left( X_{i,j}^{mod} - X_{i,j}^{obs} \right) \quad (3)$$

with  $X_{i,j}^{mod}$  and  $X_{i,j}^{obs}$  the modelled and observed chemical compositions of element  $j$  in phase  $i$ , expressed in apfu. A strong correlation is expected between two elements involved in a crystallographic substitution but they are all considered in the following as they hold different analytical uncertainties. The list of considered elements for the main solid solutions used in this study is reported in Table 1. Note that the number of elements considered for comparison increases along with the complexity of the activity model.

The magnitude of  $\Delta_{i,j}$ , the compositional difference of element  $j$  in phase  $i$ , is then compared to its relative analytical

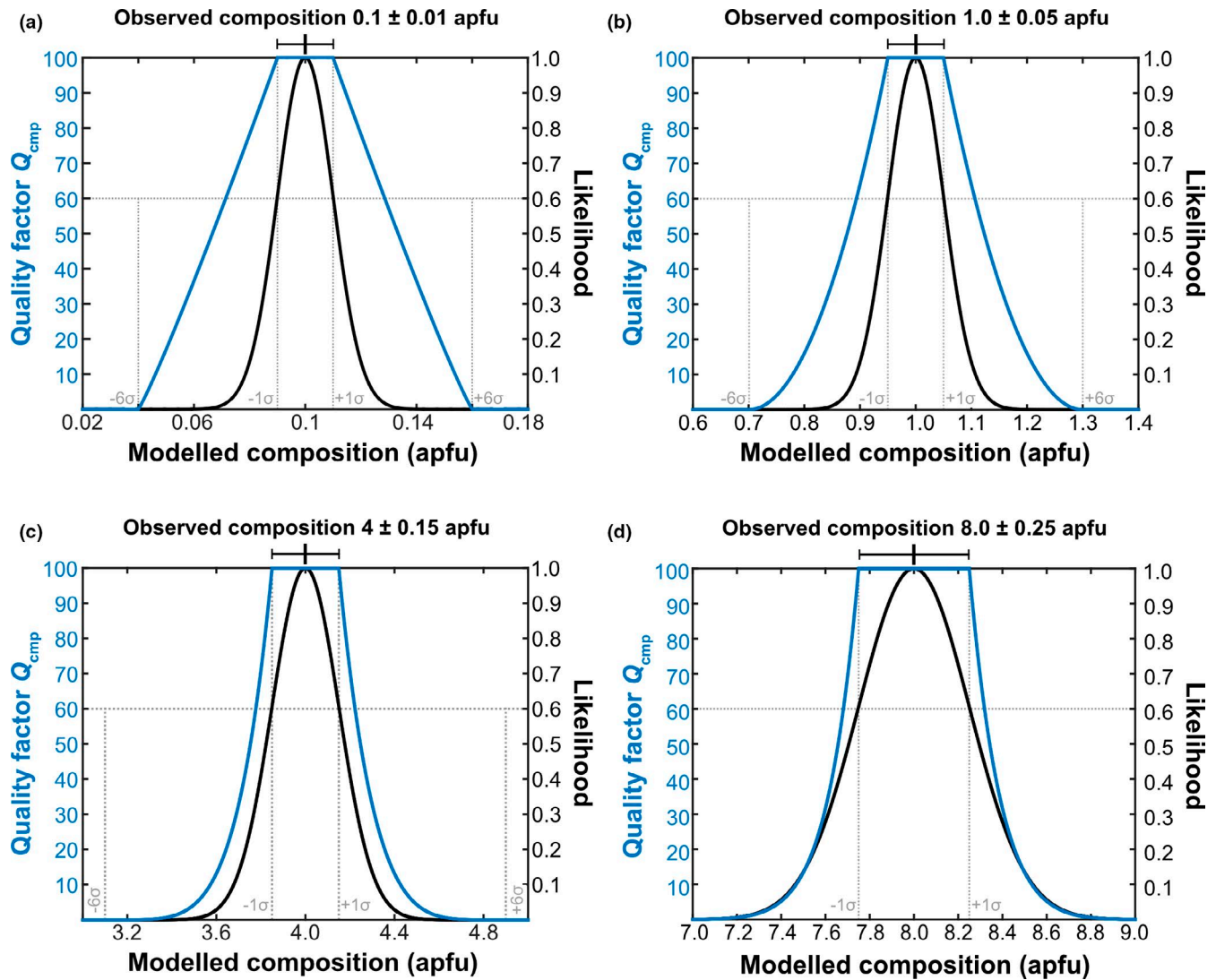


**FIGURE 4** Evolution of  $Q_{\text{cmp}}^{\text{emp}}$  with the modelled composition  $X_{ij}^{\text{model}}$  for a set of element concentration. Blue curves show the evolution of  $Q_{\text{cmp}}$  with modelled compositions and black curves the uncertainty envelope of each EPMA analysis assuming a Gaussian distribution. (a) Observed composition is  $0.1 \pm 0.01$  apfu (10% uncertainty). A modelled composition within the range 0.9–0.11 corresponds to a  $Q_{\text{cmp}}$  value of 100%. Modelled compositions of 0.08 and 0.06 apfu results to  $Q_{\text{cmp}}$  values of 78% and 36%. Any modelled composition equal or below 0.02 corresponds to a  $Q_{\text{cmp}}$  value of 0%. (b) Observed composition is  $1.0 \pm 0.05$  apfu (5% uncertainty). (c) Observed composition is  $4.0 \pm 0.15$  apfu (3.7% uncertainty). (d) Observed composition is  $8.0 \pm 0.25$  apfu (3.2% uncertainty)

uncertainty  $\sigma_{ij}$  (apfu). This relative uncertainty is taken as the amount of variation in composition for a set of pixels of the compositional maps assuming that they represent a homogeneous material. In practice, an area-of-interest is set for each phase allowing the reference composition  $X_{ij}^{\text{obs}}$  to be obtained using the mean value and the uncertainty  $\sigma_{ij}$  via the standard deviation (e.g.  $0.1 \pm 0.01$  apfu in Figure 4a). The relative precision obtained with this technique matches the prevision of the single-pixel estimate (see Lanari et al., 2017). Individual pixels have high relative uncertainties but accuracy is similar because the calibration is controlled by the high-precision spot analyses (Lanari et al., 2019). The high relative uncertainties

are minimized by pixel integration; 30 pixels of a locally homogeneous phase measured with a dwell time of 150 ms at 100 nA specimen current are more precise than a single spot analysis measured with dwell time of 20 s on peak and  $2 \times 10$  s background at 20 nA. A minimal relative uncertainty of 0.01 apfu is applied for elements with low concentrations (e.g. Mn in garnet or K in plagioclase) to avoid unrealistically small relative uncertainties compared to the uncertainties expected from the thermodynamic data.

The comparison of  $\Delta_{ij}$  with  $\sigma_{ij}$  involves first testing for  $1\sigma$  and  $6\sigma$  boundary conditions: if  $\Delta_{ij} \leq 1 \cdot \sigma_{ij}$ , then  $Q_{ij}^{\text{cmp}}$  is of 100% and if  $(\Delta_{ij} - \sigma_{ij}) \geq 6 \cdot \sigma_{ij}$  then  $Q_{ij}^{\text{cmp}}$  is 0%. If  $\Delta_{ij}$  stands between these boundary conditions,  $Q_{ij}^{\text{cmp}}$  is estimated using:

$$Q_{ij}^{\text{cmp}} = 100 \cdot \left( 1 - \frac{(\Delta_{ij} - \sigma_{ij})}{6 \cdot \sigma_{ij}} \right)^{X_{ij}^{\text{model}} + 1} \quad (4)$$

If two elements have the same degree of fitting, the exponent  $X_{ij}^{\text{model}} + 1$  devalues elements with high concentrations (Figure 4). This approach is roughly comparable to the activity of crystallographic sites having a high multiplicity. The addition of +1 is needed to avoid poorly fitting elements with  $X_{ij}^{\text{model}} < 1$  apfu to be systematically biased towards higher values. Figure 4 shows the behaviour of  $Q_{ij}^{\text{cmp}}$  with varying  $X_{ij}^{\text{model}}$ . The relative analytical uncertainty  $\sigma_{ij}$  obtained from the measured compositional map results in a plateau with a likelihood of 1. The plateau becomes broader as the uncertainty increases proportional to the element concentration (Figure 4). Therefore, a larger mismatch between model and observation is permitted for highly concentrated elements than for low concentrated elements.

The final compositional evaluation criterion  $Q_{\text{cmp}}$  is obtained by averaging the individual  $Q_{ij}^{\text{cmp}}$  for the  $l$  matching phases:

$$Q_{\text{cmp}} = \sum_i v_i^{\text{norm}} \sum_j \frac{Q_{ij}^{\text{cmp}}}{r} \quad (5)$$

Similarly to the mineral modes,  $Q_{\text{cmp}}$  is calculated only for the quality factors of each matching phase  $Q_i^{\text{cmp}}$ . In addition, the  $Q_i^{\text{cmp}}$  are weighted by the normalized volume fraction of the modelled matching phases  $v_i^{\text{norm}}$  (see Equation 5). Hence,  $Q_i^{\text{cmp}}$  of major phases with higher modes are higher ranked than minor and accessory phases. The values of  $Q_{\text{cmp}}$  in different stability fields should not be compared against each other, because the weighting makes  $Q_{\text{cmp}}$  strongly dependent on the number of matching phases.

## 2.4 | Global evaluation

Different statistical strategies can be used to assess the global quality of the model  $Q_{\text{total}}$  based on a combination of  $Q_{\text{asm}}$ ,  $Q_{\text{vol}}$  and  $Q_{\text{cmp}}$ . A general method is proposed and referred to as the *default global evaluation*  $Q_{\text{total1}}$ . It consists of a general formalism applying  $Q_{\text{asm}}$  to weight  $Q_{\text{vol}}$  and  $Q_{\text{cmp}}$ . It is defined as:

$$Q_{\text{total1}} = \frac{Q_{\text{asm}} + Q_{\text{vol}} \cdot Q_{\text{asm}} + Q_{\text{cmp}} \cdot Q_{\text{asm}}}{3} \quad (6)$$

Such global evaluation method can be used to quantitatively compare the model evaluation for two different databases. The formulation of Equation 6 incorporates weights for  $Q_{\text{vol}}$  and  $Q_{\text{cmp}}$  because both  $i$  are computed only for the matching phases (see above). It is explicitly supposed that

$Q_{\text{asm}}$  is the most important *model quality factor*, followed by  $Q_{\text{vol}}$  and  $Q_{\text{cmp}}$ . In practice,  $Q_{\text{vol}}$  has higher weight than  $Q_{\text{cmp}}$ , because quality of  $Q_{\text{cmp}}$  is a function of the applied solid solution model (with all its uncertainties and limits) of the modelled solid solution phase whereas the mode of a solution phase is often less significantly influenced by the end-member fractions (e.g. the extent of Tschermak and Fe–Mg substitutions in white mica in equilibrium with chlorite, quartz and albite do not affect its mode which is rather controlled by the amount of K available in the system).

Alternatively, an adaptive weighting scheme can be used (referred to as *adaptive evaluation*), which involves user-specific weights  $w_{\text{asm}}$ ,  $w_{\text{vol}}$  and  $w_{\text{cmp}}$

$$Q_{\text{total2}} = w_{\text{asm}} \cdot Q_{\text{asm}} + w_{\text{vol}} \cdot Q_{\text{vol}} + w_{\text{cmp}} \cdot Q_{\text{cmp}} \quad (7)$$

The specific weights can be set by the user (software option). They can vary from case to case and are problem dependent. This alternative method is used for cross-checking the results of the global evaluation and to explore the sensitivity of any model quality factors. For instance, it is possible to neglect one model quality factor by fixing the corresponding weight to zero. Nevertheless, it is recommended to report the global evaluation value  $Q_{\text{total1}}$  as default benchmark.

## 3 | ANTIDOTE—IN SEARCH OF THE ‘OPTIMAL’ $P$ – $T$ CONDITIONS

The evaluation of correlation between the observations and predictions of the equilibrium models is a non-linear optimization problem. The program ANTIDOTE contains several routines, referred to as ‘recipes’, to investigate how the model quality factors evaluated by BINGO change within the  $P$ – $T$ – $X$  range of the model. A graphical user interface is developed in MATLAB<sup>®</sup> including all recipes for investigating compositional maps. The software XMAPTOOLS 3.2.1 was used to standardize the X-ray maps; the add-on BINGO-ANTIDOTE 1.1.2 to investigate the LBC compositions using BINGO-ANTIDOTE. For modelling, the GEM are performed by THERIAK (de Capitani & Brown, 1987) and were implemented into MATLAB<sup>®</sup> using the strategy of the add-on THERIAK\_D (Duesterhoeft & de Capitani, 2013). Five groups of recipes are defined in Table 2 and briefly described in the following.

### 3.1 | Global inversion and ‘optimal’ $P$ – $T$ – $X$ conditions

The goal of this group of recipes is to constrain both the minimum and the shape of an objective function  $f$  defined as:

**TABLE 2** List of recipes available in ANTIDOTE 1.1 (reference, name, description)

Global inversion and optimal $P$ - $T$ - $X$ conditions		
#1	Find optimal $P$ - $T$ (- $X$ )	Search routine performing a global optimization of $P$ , $T$ , possibly including the molar amounts of some components of the bulk composition such H, C or O and activity variables of fluids and gases: $a_{\text{H}_2\text{O}}$ , $a_{\text{CO}_2}$ , $f(\text{O}_2)$
#2	$P$ - $T$ map of $Q$ factors	Mapping function for mapping the quality factor functions ( $Q_{\text{asm}}$ , $Q_{\text{vol}}$ , $Q_{\text{cmp}}$ , $Q_{\text{cmp}}$ of individual phases and $Q_{\text{total}}$ ) in the $P$ - $T$ space
#3	$P$ - $T$ uncertainty	Search routine evaluating the local shape of the objective function ( $-Q_{\text{total}}$ , see text) and calculating an uncertainty envelope
Single-phase thermobarometry		
#4	Find optimal $P$ - $T$ (single phase)	Search routine performing single-phase thermobarometry via $P$ - $T$ optimization
#5	$P$ - $T$ map (single phase)	Mapping function generating $Q_{\text{cmp}}$ maps for single phase
#6	$P$ - $T$ uncertainty (single phase)	Search routine for calculating an uncertainty envelope
Sensitivity tests on the results of GEM		
#7	Bulk sensitivity	Evaluation of the model sensitivity to the bulk composition at fixed $P$ - $T$ by randomly changing the domain shape
#8	$P$ - $T$ sensitivity	Evaluation of the model sensitivity to $P$ - $T$ conditions under fixed bulk composition by randomly changing $P$ - $T$
#9	$P$ - $T$ -bulk sensitivity	Evaluation of the model sensitivity to the bulk composition and $P$ - $T$ conditions by randomly changing the domain shape and the $P$ - $T$ conditions
Textural investigation		
#10	Floating window (fixed $P$ - $T$ , variable bulk)	Model evaluation at fixed $P$ - $T$ for variable LBC calculated along a path using a rectangular floating window and a moving average scheme
#11	Scanning window (find optimal $P$ - $T$ , variable bulk)	Search routine applied to a scanning window to quantify how local heterogeneities in compositions can affect the optimal $P$ - $T$ conditions
#12	Growing window (find optimal $P$ - $T$ , variable bulk)	Search routine applied to a growing window for the quantification of size-related effects on the model quality
#13	Chemical potential mapping (fixed $P$ - $T$ )	Mapping of chemical potential landscapes
Optimization of compositional and activity variables		
#14	Scanning H (fixed $P$ - $T$ )	Optimization of compositional variables at fixed $P$ - $T$
#15	Scanning C (fixed $P$ - $T$ )	
#16	Scanning O (fixed $P$ - $T$ )	

$$f(P, T, X_{\text{bulk},j=1}, X_{\text{bulk},j=2}, \dots, X_{\text{bulk},j}) = -Q_{\text{total}} \quad (8)$$

with  $X_{\text{bulk},j}$  the concentration of component  $j$  in  $X_{\text{bulk}}$ . Both  $Q_{\text{total}1}$  and  $Q_{\text{total}2}$  parameters can be used to set the objective function. They can provide similar or different minima depending on the degree of equilibration of the investigated sample. Inverting  $f$  is a non-linear optimization problem for which the derivatives are unknown and therefore requires a heuristic search method (Lanari et al., 2017).

*Recipe #1* contains a search routine performing a global optimization of  $P$ ,  $T$  along with some components of the bulk composition such as the molar amounts of H, C and O. Optimization is not straightforward because it can contain biases such as the convergence to local minima that are different from the global minimum. To reduce such effects, a two-step search method is used here. The first step consists of regularly mapping the objective function in  $P$ - $T$  using a small

grid ( $10 \times 10$  by default) and then in the  $P$ - $T$ - $X$  multidimensional space of the stability field having the highest  $Q_{\text{asm}}$ . The optimization is stopped if  $f$  is flat along any dimension, that is, if there are too many free parameters that are optimized for the given set of constraints. The parameters corresponding to the minimum value of  $f$  are then used as initial value for the second *optimization step* applying the algorithm of Nelder and Mead (1965), a downhill simplex method. The minimum value of  $f$  found by the search routine is taken as the 'optimal' solution of the problem. The local variability of  $f$  can be investigated by *Recipe #3* using the refinement procedure of Lanari et al. (2017) coupled to a multi-step random sampling procedure refining the shape of the domain within a given uncertainty range. The first Monte Carlo sampling step samples the whole  $P$ - $T$  range and finds the  $P$ - $T$  points fitting the uncertainty criterion (2% by default). An uncertainty range is drawn from these  $P$ - $T$  points. The next Monte Carlo

sampling steps refine the corner positions of this uncertainty range.

*Recipe #2* allows the objective function  $f$  and each model quality factor such as  $Q_{\text{asm}}$ ,  $Q_{\text{vol}}$ ,  $Q_{\text{cmp}}$  or  $Q_i^{\text{cmp}}$  to be mapped in the  $P$ – $T$  space. Such maps can for example be used to identify mineral phases that were not fully re-equilibrated at the peak conditions (e.g. plagioclase in the example of Lanari & Duesterhoeft, 2019).

### 3.2 | Single-phase thermobarometry

Optimization can also be performed individually for each solid solution mineral phase. This group of recipes provides a solution for the application of single-phase thermobarometry without considering the co-existing phases based on the objective function  $f^*$  defined as:

$$f^*(P, T) = -Q_i^{\text{cmp}} \quad (9)$$

A dedicated search routine based on the simplex algorithm is provided in *Recipe #4*. The optimal  $P$ – $T$  solution of a given phase corresponds to the best intersection of all the element isopleths of the solution (see Table 1) with a robust weighting scheme (see Equation 4). The objective function  $f^*$  can also be mapped and contoured in the  $P$ – $T$  space for a given uncertainty range using *Recipe #5* and *Recipe #6* respectively (similar to *Recipe #2* and *#3*).

### 3.3 | Sensitivity tests on the results of GEM

The sensitivity of GEM-based results to key parameters such as  $P$ – $T$  or  $X_{\text{bulk}}$  can be quantified using the scoring strategy of BINGO. The choice of the area-of-interest in a given sample is for example arbitrary and dictates  $X_{\text{bulk}}$ . Sensitivity tests are performed in ANTIDOTE via a series of Monte Carlo simulations (e.g. 2,000 permutations) tracking the dispersion of the predicted mineral modes and compositions at the  $2\sigma$  level. For example, *Recipe #7* tests the sensitivity of GEM-based forward models to the input bulk composition by randomly changing the shape of the area-of-interest (e.g. Lanari & Engi, 2017). The sensitivity of GEM to changes in  $P$ – $T$  can be quantified using *Recipe #8*. The dispersion ( $\pm 2\sigma$ ) of the mineral modes predicted by the equilibrium model with variable bulk or  $P$ – $T$  is visualized in histograms for each phase.

### 3.4 | Textural investigation

The goal of this group of recipes is the quantification of changes caused by spatial heterogeneities and different local

mineral assemblages. The floating window (*Recipe #10*) strategy can be used to quantify the effects of changing local bulk compositions on the model outcome along a moving, rectangular LBC-polygon on the compositional map and by applying a moving average scheme (like a ‘raft floating on a river’). The size of the moving window can be adjusted depending on the wavelength of the observable, that is, the grain size or the size of compositional gradients. For a defined number of steps (30 by default), the LBC is recalculated for each step along the path on the map. Then, the evaluation criteria for each LBC and  $Q_{\text{cmp}}$  of each mineral are calculated and plotted against the number of steps. If the resulting gradients are flat, it may indicate that the domain is well equilibrated (from a textural and chemical point of view). But if steep gradients exist, it may point to different equilibrium conditions preserved in distinct local domains. This recipe is similar to the example of Lanari and Engi (2017), except that the polygon is not growing (see their fig. 15a,b).

*Recipes #11–13* involve *systematic rastering* across the compositional map, and the calculation of optimal  $P$ – $T$  conditions for each raster (resp. ‘window’). The scanning window (*Recipe #11*) determines ‘optimal’  $P$ – $T$  conditions for a given amount of half overlapping map sections equal in size. Alternatively, the growing window (*Recipe #12*) derives ‘optimal’  $P$ – $T$  conditions for a specific amount of windows, starting with a small window in the middle of map systematically increasing until the window hits the map frame. Each window has to envelop several minerals including solid solutions to avoid a flat objective function. *Recipe #13* is based on a grid algorithm that generates maps of chemical potential gradient landscapes calculated at fixed pressure and temperature (see Appendix 1). Information about possible metastability of phases at given  $P$ – $T$  can be obtained as well as direction of element/oxide diffusion.

### 3.5 | Optimization of compositional variables

The model quality factors evaluated by BINGO can be scanned at fixed  $P$ – $T$  conditions along a given range of H (*Recipe #14*), C (*Recipe #15*) or oxygen fugacity (*Recipe #16*). The resulting diagrams illustrate how the model quality factors change with oxygen fugacity (O), the amount of hydrous phases or melt (H), or the  $X_{\text{CO}_2}$  of the fluid (C). An example in which the amount of hydrogen is optimized is given in Lanari and Duesterhoeft (2019). Optimization of a chemical variable together with variable  $P$  and  $T$  is complex in terms of high amount of possible solutions (local minima) that are petrologically equal in value and are only mathematically distinguishable. Evaluation of the local minima can only be done manually and requires a high understanding of the investigated sample.

## 4 | APPLICATION EXAMPLE—SAMPLE HAL104

To illustrate the usefulness of BINGO-ANTIDOTE, the bulk rock composition and EPMA mineral compositions of a garnet–biotite gneiss from the Central Metasedimentary Belt in the southwestern Canadian Grenville Province were used. This sample comes from a well-known outcrop near the village of West Guilford (Ontario) and is located between the Redstone and Dysart thrust sheets. The outcrop is part of a continuous unit on Hanmer's (1989) geological map labelled 'Poc: undifferentiated sillimanite-kyanite-garnet-ortho-amphibole-cordierite gneiss'. Hanmer (1988) interpreted this unit as metapelitic and suggested minimum metamorphic conditions of 650°C and 0.6 GPa. Later, Anovitz and Essene (1990) proposed pressure conditions of  $0.72 \pm 0.05$  GPa for this unit, obtained using the GASP geobarometer (see sample HAL 83C 38). Calcite–graphite carbon isotope thermometry on surrounding marbles revealed a maximal temperature between 661 and 705°C (Dunn et al., 2019). Markley, Dunn, Jercinovic, Peck, and Williams (2018) reported U–Pb ages for monazite from the same outcrop (see sample West Guilford HA13). The first age population of 1,095–1,080 Ma was interpreted as reflecting monazite growth during prograde metamorphism, whereas the second age population of 1,050–1,045 Ma was interpreted as reflecting re-equilibration during a late retrogression stage after cooling and/or decompression. The older age is in line with the U/Pb zircon age of  $1,078 \pm 3$  Ma of McEachern and van Breemen (1993). The main mineral assemblage of sample HAL104 is made of quartz, plagioclase, biotite, garnet, sillimanite and minor staurolite. In contrast to other layers of this unit, neither kyanite, gedrite nor potassic feldspar was observed. Textural observations suggest first that sillimanite and staurolite did not form in equilibrium. Staurolite forms tiny, rounded crystals in plagioclase and in close relationship with biotite. In this sample, two local assemblages can be related to two distinct metamorphic stages: (a) peak metamorphism with the inferred assemblage garnet (core)–plagioclase–biotite–sillimanite–quartz and (b) a retrograde stage garnet(rim)–biotite–staurolite±plagioclase±quartz.

### 4.1 | Inverse modelling

Multi-equilibrium geothermobarometry was performed using the winTWQ2007 software (Berman, 2007) and the modified internally consistent thermodynamic database 'JUN92' after Berman (1988; Figure 5a). A total of eight equilibria including a set of three independent equilibria (blue curves) were plotted using the mineral compositions reported in Table 3. Assuming chemical equilibrium between the garnet rims,

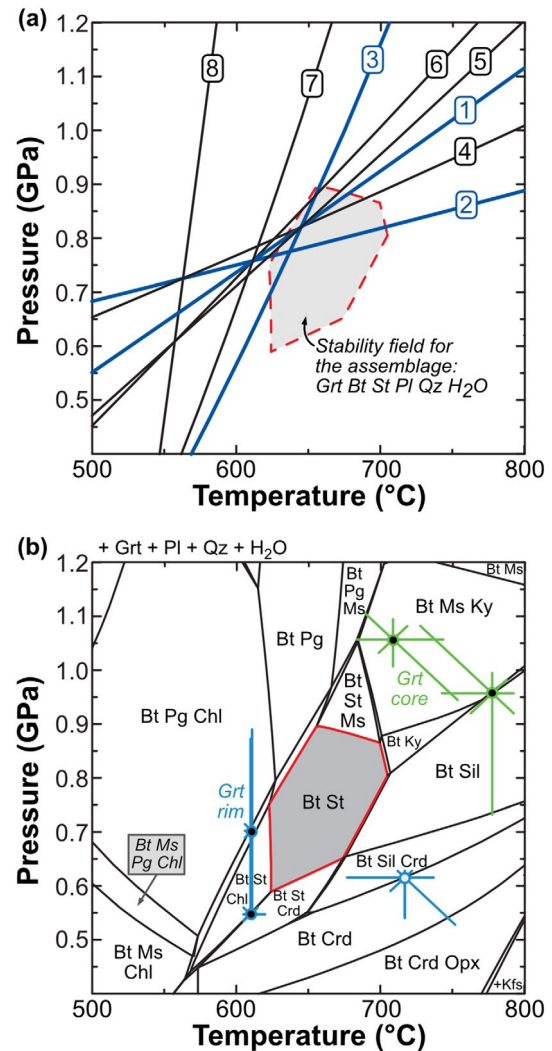


**FIGURE 5** Thermobarometric investigation of sample HAL104 based on (a) multi-equilibrium thermobarometry, (b) isochemical phase diagram combined with isopleth thermobarometry using the same thermodynamic database JUN92. (a) Multi-equilibrium model using the mineral compositions of garnet rim and the surrounding biotite to calculate activities; the mineral compositions are reported in Table 3. The curves of the independent set of equilibria selected in this study are plotted in blue. Equilibria: (1) Grs+Qz+2Sil=3An; (2) 96Sil+8Prp+25Grs+8Ann+12H<sub>2</sub>O=75An+8Phl+6St; (3) 25Qz+6St=46Sil+8Alm+12H<sub>2</sub>O; (4) 96Sil+25Gr+8Alm+12H<sub>2</sub>O=75An+6St; (5) 6St+46Qz+23Grs=8Alm+69An+12H<sub>2</sub>O; (6) 6St+46Qz+8Phl+23Grs=8Ann+69An+8Prp+12H<sub>2</sub>O; (7) 8Phl+25Qz+6St=46Sil+8Prp+8Ann+12H<sub>2</sub>O; (8) Phl+Alm=Ann+Prp. (b) isochemical phase diagram computed in the chemical system SiO<sub>2</sub>–Al<sub>2</sub>O<sub>3</sub>–FeO–MnO–MgO–CaO–Na<sub>2</sub>O–K<sub>2</sub>O–H<sub>2</sub>O. The P–T conditions of garnet core (green) and rim (blue) compositions were obtained using GRTMOD. Several solutions statistically equivalent are reported for each case

adjacent biotite, staurolite and plagioclase (retrograde stage), the P–T conditions of 0.75–0.82 GPa at 610–630°C were obtained based on the convergence of the three independent equilibria.

**TABLE 3** List of the bulk rock and mineral compositions used for the calculation of Figures 5 and 6

No.	Bulk composition	Pl	St	Grt-rim	Bt-2	Grt-core	Bt-1
		2-322	2-323	2-385	2-387	1-319	2-268
SiO <sub>2</sub>	70.1	67.2	27.2	38.6	37.2	39.1	36.9
TiO <sub>2</sub>	0.4	0.0	0.8	0.0	2.3	0.0	2.6
Al <sub>2</sub> O <sub>3</sub>	13.4	20.3	52.7	21.5	17.4	22.3	17.3
FeO	6.1	0.3	13.5	33.5	13.6	28.2	14.5
MnO	0.1	0.0	0.1	1.4	0.1	1.1	0.6
MgO	3.3	0.0	3.3	6.2	15.0	9.6	15.5
CaO	0.4	1.2	0.0	0.2	0.0	0.4	0.0
Na <sub>2</sub> O	2.8	10.8	0.0	0.0	0.2	0.0	0.2
K <sub>2</sub> O	1.4	0.1	0.0	0.0	9.6	0.0	9.6
P <sub>2</sub> O <sub>5</sub>	0.1	—	—	—	—	—	—
Total	99.2	99.8	97.6	101.3	95.3	100.8	95.7

## 4.2 | Forward modelling

A  $P$ – $T$  isochemical phase diagram for sample HAL104 (Figure 5b) was calculated in the system SiO<sub>2</sub>–Al<sub>2</sub>O<sub>3</sub>–FeO–MnO–MgO–CaO–Na<sub>2</sub>O–K<sub>2</sub>O–H<sub>2</sub>O using THERIAK-DOMINO (de Capitani & Brown, 1987; de Capitani & Petrakakis, 2010) and the same thermodynamic database JUN92. The components SiO<sub>2</sub> and H<sub>2</sub>O were considered to be in excess. The observed mineral assemblage (Grt, Bt, St, Plg, aQz) is modelled in a  $P$ – $T$  field ranging between 620–700°C and 0.6–0.9 GPa. Between 0.65 and 0.8 GPa and towards higher temperatures, sillimanite becomes stable at the expense of staurolite. The results are in line with the results of the inverse model and support the assumption that the minerals characteristic of the retrograde stage were in equilibrium at  $625 \pm 25^\circ\text{C}$  and  $0.75 \pm 0.15$  GPa in this rock.

## 4.3 | Simple ITM using GRTMOD

The  $P$ – $T$  conditions of garnet formation were modelled using the program GRTMOD (Lanari et al., 2017), which is an ITM based on the inversion of an objective function that compares the observed and modelled garnet compositions. The same bulk composition and thermodynamic database were used. The results obtained for the compositions of garnet core (green) and rim (blue) are shown in Figure 5b. Several solutions can be found as the strategy involves up to four optimizations from different starting points (see Lanari & Duesterhoeft, 2019 for an example containing two solutions that are equivalent from a statistical point of view). For sample HAL104, two and three solutions with similar residuals were found for garnet core and rim. For the rim, two of them (at 610°C) overlap within

uncertainties and lie in the staurolite stability field. The third solution was obtained at higher temperature (717°C) in the sillimanite stability field. The first two solutions are in line with the multi-equilibrium geothermobarometry and petrographic observations and are interpreted as the  $P$ – $T$  conditions related to the retrograde stage. The two solutions for garnet core are overlapping within uncertainty at temperatures  $>700^\circ\text{C}$  and pressure  $>0.75$  GPa. Solution 2 is preferred here as it falls within the sillimanite stability field. No kyanite was observed in this sample, but the presence of kyanite was reported in the surrounding rocks of this unit (see above). The amount of solutions with small residuals together with the relatively large uncertainties envelopes show that the garnet composition is, in this case, largely limited by the bulk rock composition (i.e. no significant variation in garnet composition is possible within this  $P$ – $T$  range).

## 4.4 | BINGO

The same mineral compositions, bulk rock composition and thermodynamic database were used as input for BINGO. The following mineral modes were approximated for the retrograde stage based on petrographic observations: quartz (45 vol.%), plagioclase (25%), biotite (15%), garnet (10%) and staurolite (5%). The model quality factor  $Q_{\text{asm}}$  mimics the isochemical equilibrium phase diagram of Figure 5b and a value of 100% is reached within the stability field where the observed assemblage (Grt, Bt, St, Pl, Qz) is modelled (Figure 6). The approximation of the modes is interpreted as reasonable as suggested by the high value of  $Q_{\text{vol}}$  ( $>90\%$ ) with a maximum of 96% at 635°C and 0.81 GPa. The maximum value of  $Q_{\text{cmp}}$  within the stability field of the assemblage ( $Q_{\text{asm}} = 100\%$ ) is 84% at 625°C and 0.76 GPa, and in agreement with the

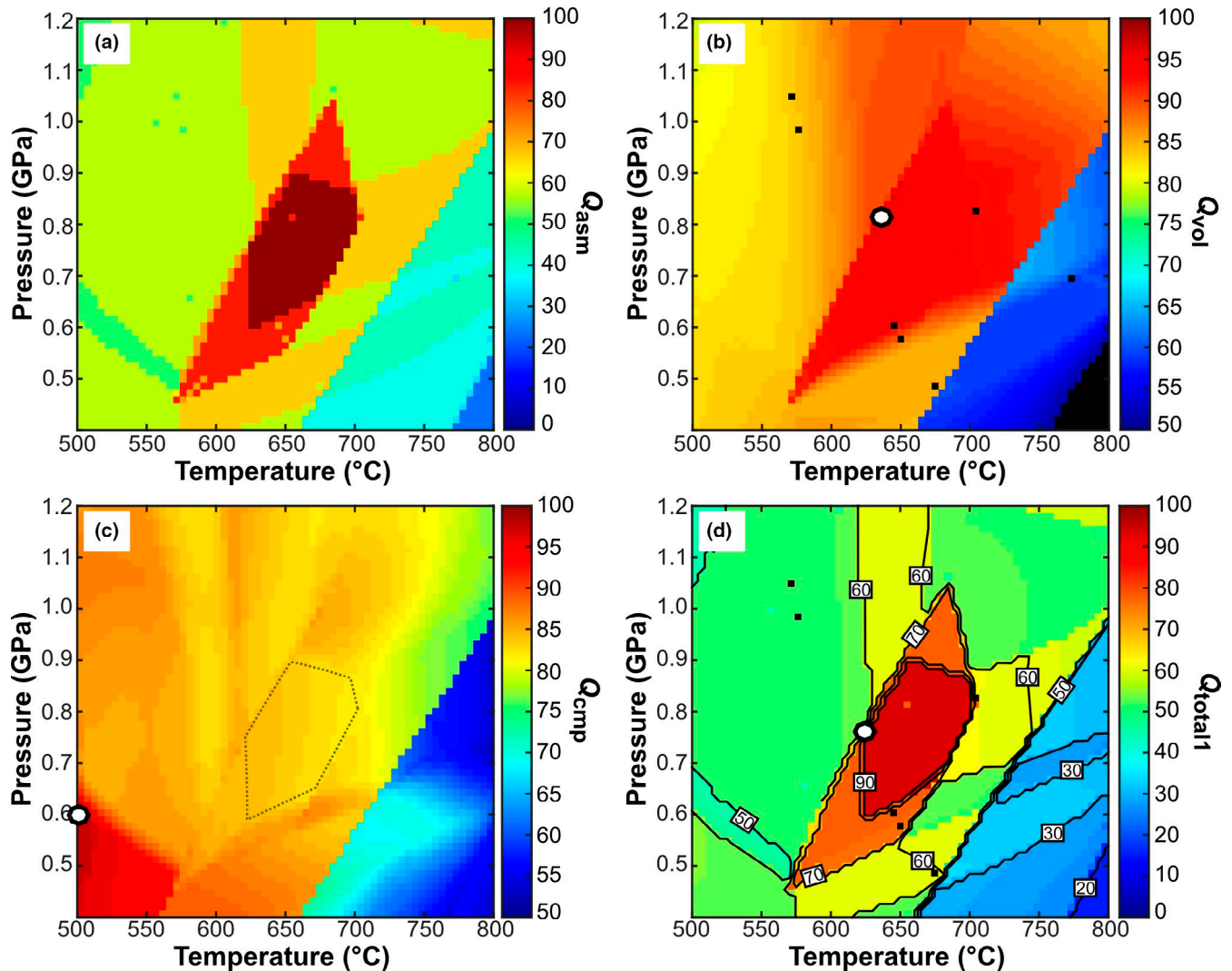


**FIGURE 6** Results of the standalone version of Bingo-Antidote shown as  $P$ – $T$  maps of quality factor for (a)  $Q_{asm}$ , (b)  $Q_{vol}$ , (c)  $Q_{cmp}$  and (d)  $Q_{total1}$ . The same mineral compositions, bulk rock composition and thermodynamic database were used as for Figure 5. The circle symbols in (b), (c) and (d) indicate the  $P$ – $T$  conditions of the maximum value for each quality factor plot. The dashed domain in (c) shows the  $P$ – $T$  region with  $Q_{cmp} = 100\%$

conditions of 0.75–0.8 GPa and 600–700°C obtained above. Finally, the global evaluation factor  $Q_{total1}$  is 93% at 625°C and 0.76 GPa ( $Q_{asm} = 100\%$ ;  $Q_{vol} = 95\%$ ;  $Q_{cmp} = 84\%$ ). The results obtained by BINGO are identical to the results obtained by multi-equilibrium geothermobarometry and isochemical phase diagram combined with garnet isopleths. This benchmarking test demonstrates the mathematical validity of the scoring technique implemented in BINGO. However, the petrological reliability of this result highly depends on the petrographic interpretation, as discussed below.

#### 4.5 | BINGO-ANTIDOTE applied to compositional maps—‘optimal’ $P$ – $T$ conditions

To illustrate the usefulness of ANTIDOTE, X-ray maps of the sample HAL104 (Figure 7a) were acquired at the Institute

of Geological Sciences of the University of Bern using a JEOL JXA-8200 superprobe with an accelerating voltage of 15 KeV, specimen current of 100 nA, beam size of 1  $\mu$ m and a step size of 20  $\mu$ m. The maps were standardized with XMAPTOOLS 3.2.1 (Lanari et al., 2014) using spot analyses as internal standards and the calibration method described in Lanari et al. (2019). The compositional maps of a few diagnostic elements, end-member proportions or elemental ratios are provided in Figure 7. The observed mineral modes in the mapped area are 40 vol.% for quartz, 30% for plagioclase, 7% for garnet, 17% for biotite and 6% for sillimanite. Minor ilmenite, pyrite and Fe-oxide (<0.01 vol.%) and a single-pixel of staurolite (over 1,000,000) are not considered in the following. This example illustrates the stark difference that can exist between the rock volume used to determine the bulk rock composition that contained up to 5 vol.% of staurolite (see above) and the mapped area containing less

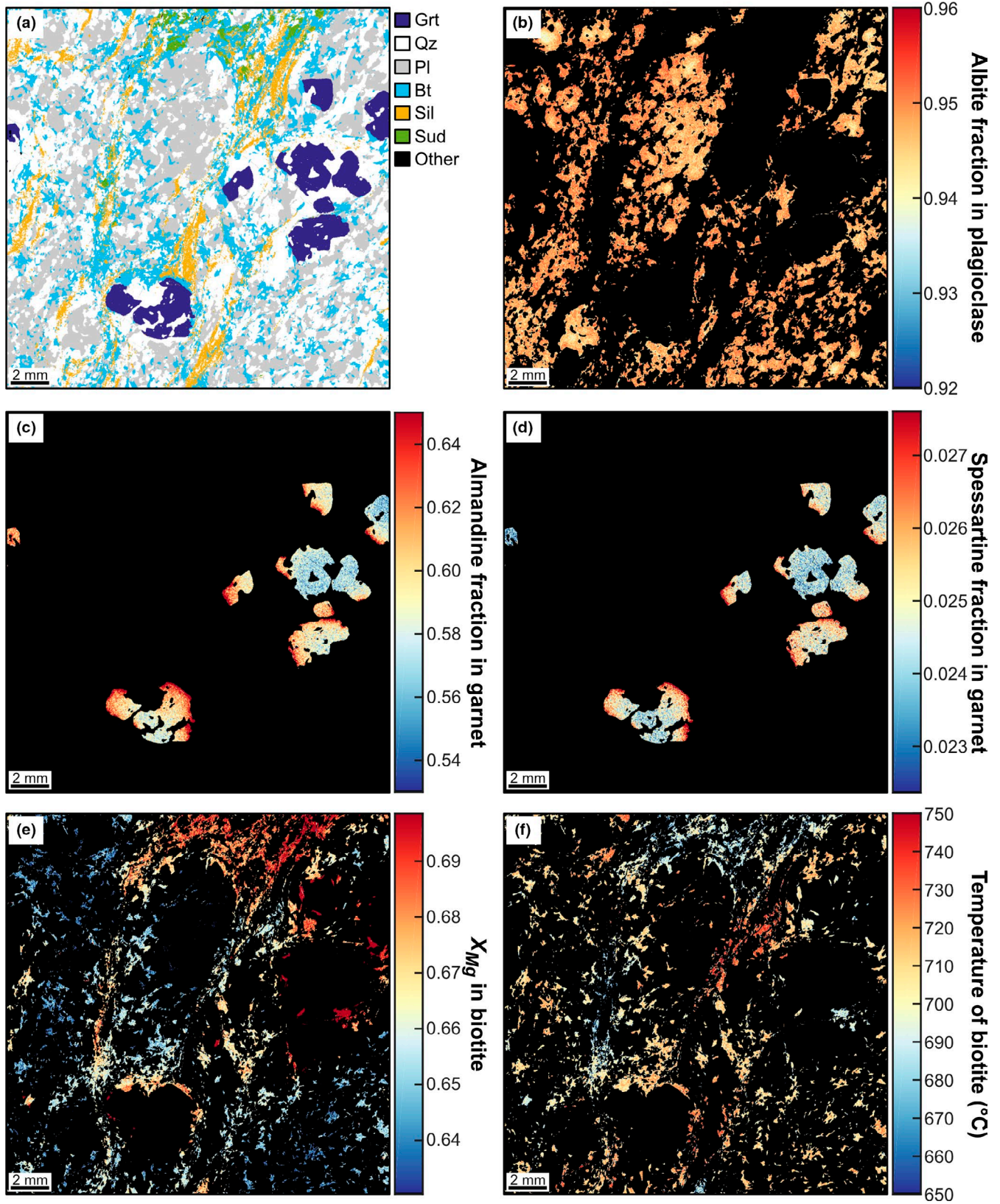


**FIGURE 7** Selection of quantitative compositional maps, a map of mineral distribution and Ti-in-biotite temperatures for sample HAL104. (a) Mineral distribution map; 'Other' indicates accessory minerals and staurolite (see text) and represent less than 0.01% of the mapped area. (b–e) compositional maps of (b) albite fraction in plagioclase, (c) almandine and (d), spessartine fractions in garnet, (e)  $X_{Mg}=(Mg)/(Mg+Fe)$  in biotite and temperature map of (f) biotite obtained using the calibration Ti-in-biotite of Henry, Guidotti, and Thomson (2005)

that 0.01% of staurolite. Thin garnet rims (<500  $\mu\text{m}$ ) exhibit a higher almandine component with near-rim Mn kick-up characteristic of retrograde diffusion (Kohn & Spear, 2000). Cryptocrystalline sudoite partly sericitized to a fine-grained white mica along fractures and grain boundaries is present in the upper part of the mapped area, where garnet is notably absent (Figure 8a). Biotite grains in this area have higher  $X_{\text{Mg}}$  values (Figure 8e) and lower Ti contents (corresponding to lower temperature in Figure 8f). Sudoite is a low-temperature di-trioctahedral chlorite (Lanari, Wagner, & Vidal, 2014)

and is interpreted here as the replacement product of former cordierite. Cordierite could have formed in local equilibrium with Mg-rich biotite during the retrograde stage, that is, after the peak conditions. The pixels belonging to sudoite were excluded for the estimation of local bulk compositions (software option) as they no longer reflect the original composition of (possible) former cordierite.

A homogeneous domain of  $\sim 20 \times 20$  mm was used to determine the reference local bulk composition of this sample ( $\text{LBC}_1$  in Figure 8a). The calculations were performed in the

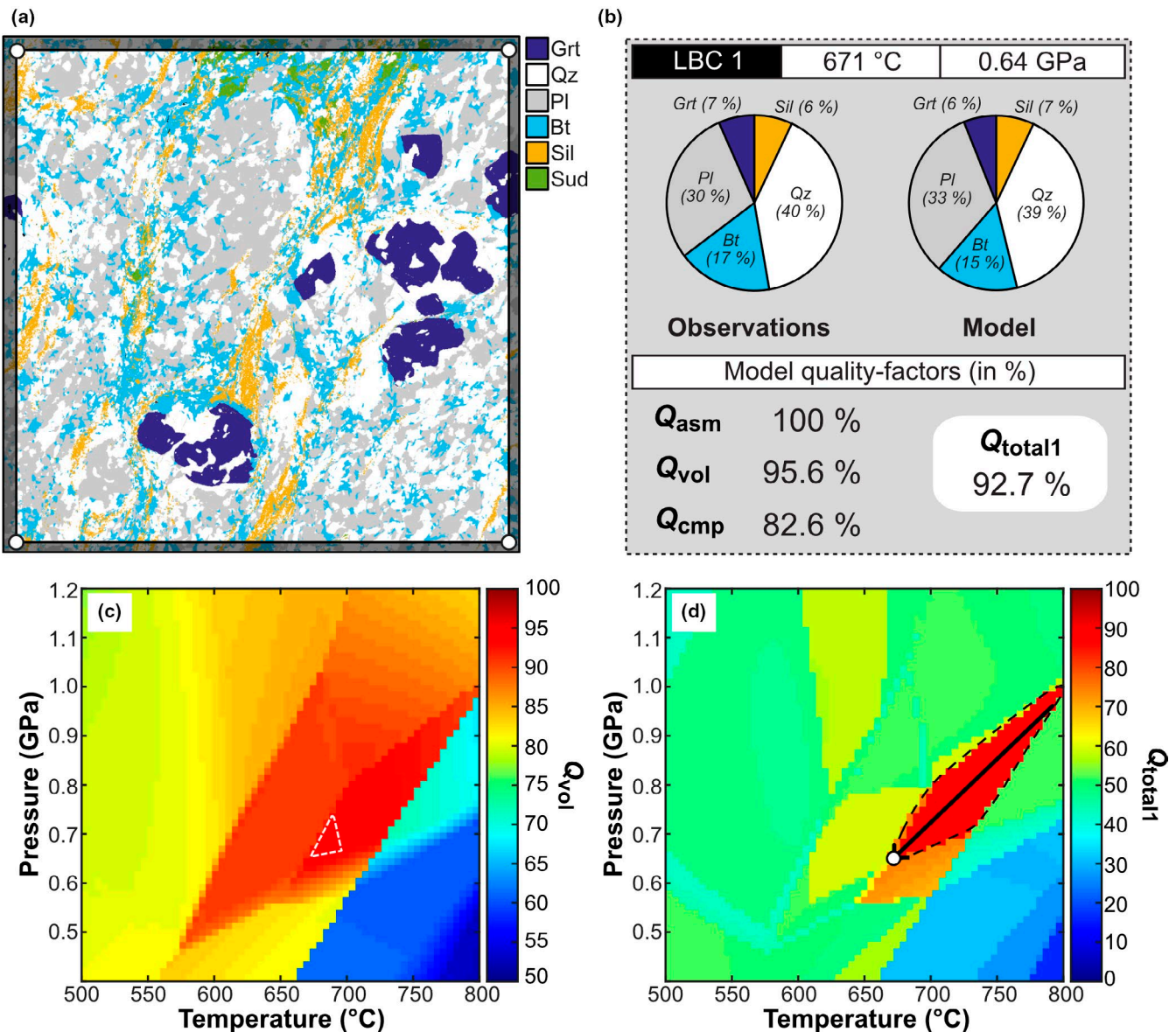


**FIGURE 8** ‘Optimal’  $P$ - $T$  conditions obtained using Bingo-Antidote. (a) Mineral distribution map showing the area-of-interest used to determine the local bulk composition  $\text{LBC}_1$  (see text):  $\text{SiO}_2$ : 70.25 wt%;  $\text{Al}_2\text{O}_3$ : 15.37%;  $\text{FeO}$ : 5.24%;  $\text{MnO}$ : 0.15%  $\text{MgO}$ : 3.47%;  $\text{CaO}$ : 0.38%;  $\text{Na}_2\text{O}$ : 3.38%;  $\text{K}_2\text{O}$ : 1.77%. (b) Results of ITM based on  $\text{LBC}_1$ . Observed/modelled mineral modes and quality factors for the optimal solution of 671°C and 0.64 GPa obtained with recipe #1 of Antidote. The compositions of garnet core and matrix biotite were used. (c, d)  $P$ - $T$  maps of quality factor  $Q_{\text{vol}}$  and  $Q_{\text{total1}}$ . The dashed area in (c) shows the region with  $Q_{\text{vol}} > 95\%$ . In (d), the uncertainty region (black dashed area) obtained using an arbitrary threshold of 2% is identical to the stability field of the peak assemblage Grt+Bt+Sil+Pl+Qz

system  $\text{SiO}_2\text{--Al}_2\text{O}_3\text{--FeO--MnO--MgO--CaO--Na}_2\text{O--K}_2\text{O--H}_2\text{O}$  first using the database JUN92. Later the BED92 and tc55 databases are used for comparison. The choice of the thermodynamic database has a pedagogical approach and do not reflect a preference for the investigated sample. The application of these three databases makes it possible to identify technical details of BINGO-ANTIDOTE and significant differences that can be quantified by the program. Nevertheless, the difference in the outcome (in terms of petrological interpretations) of these and newer databases is marginal.

For the peak mineral assemblage, optimal  $P\text{--}T$  conditions of 671°C and 0.64 GPa were obtained with *Recipe #1* within the stability field Grt, Bt, Sil, Qz, Pl, using the composition of garnet core and matrix biotite (Figure 8b). The model quality factors at these conditions are  $= Q_{\text{asm}} 100\%$ ,  $Q_{\text{vol}} = 95.6\%$ ,  $Q_{\text{cmp}} = 82.6\%$  and  $Q_{\text{total}} = 92.7\%$ .

In a second step, maps of model quality factors were generated for the  $P\text{--}T$  range of 500–800°C and 0.4–1.2 GPa using *Recipe #2* and the same local bulk composition  $\text{LBC}_1$ . The inferred peak assemblage (corresponding to  $= Q_{\text{asm}} 100\%$ ) is modelled in the range of 670–800°C and 0.64–1.0 GPa. In this stability field,  $Q_{\text{vol}}$  reaches a maximum value of 95.5% (dashed line in Figure 8c). The quality of mineral compositions is lower in this stability field ( $Q_{\text{cmp}}$  value of ~82.6%) whereas higher values are found in two distinct  $P\text{--}T$  ranges, at lower  $P\text{--}T$  (500–550°C at 0.4–0.6 GPa) and higher  $P$  (680–750°C at 0.1–0.12 GPa, see  $Q_{\text{cmp}}$  map in Figure 9h). The first maximum at lower  $P\text{--}T$  is misleading since it results from the high concentration and high  $Q_{\text{cmp}}$  values of plagioclase and quartz, whereas biotite and garnet modes are approaching zero. The second maximum at higher  $P$  is more interesting because the compositions of plagioclase, garnet core and matrix biotite are matching at these conditions (Figure 9e–g). A  $P\text{--}T$  map of  $Q_{\text{total}}$  was computed and is reported in Figure 8d. At the optimal peak conditions of 671°C and 0.64 GPa, the uncertainty range obtained using *Recipe #3* follows the geometry of the stability field of the peak assemblage (Figure 8d). In this model,  $Q_{\text{asm}}$  is the dominant model quality factor. However, the evaluation of quality factors for individual mineral, especially for  $Q_{\text{cmp}}$ , can be used to identify phases that could be metastable or badly modelled (e.g. Lanari & Duesterhoeft, 2019). Such maps were generated using *Recipe #5* (Figure 9). Figure 9a–d shows the quality factor maps of garnet rim ( $\text{Grt}_2$ ) and adjacent biotite compositions ( $\text{Bt}_2$ ), which were not previously considered. These  $Q_{\text{cmp}}$  maps are shown for comparison with the results obtained from the *classical sample preparation and analytical strategy* (see Figure 5). The quality factor maps of garnet core and matrix biotite compositions are shown in Figure 9e–h. The high correlation area of  $Q_{\text{cmp}}$  for garnet rim and core vary, but are in line with the GRTMOD results (Figure 5b). From the two maps of  $Q_{\text{cmp}}$  it seems that neither plagioclase, garnet rim nor the adjacent biotite were in equilibrium with each other

during the retrograde stage, whereas the high correlation areas of  $Q_{\text{cmp}}$  of plagioclase, garnet core and matrix biotite intersect at ~700°C and 1–1.1 GPa. In both cases, the same plagioclase composition and database were used.

Considering the  $Q_{\text{cmp}}$  maps, the correlation between observed and modelled biotite composition is poorer than for garnet or plagioclase (max.  $Q_{\text{cmp}}^{\text{bt}}$  of ~35%). This suggests that the biotite solid solution model in the database is limited and cannot predict the observed composition. A more up-to-date solution model based on the Mg–Fe–Al multisite mixing model of Berman, Aranovich, Rancourt, and Mercier (2007) (incorporated in the BED92 database of Duesterhoeft, 2017) was used instead of the ideal one-site Mg–Fe mixing model of the JUN92 database. This change significantly improved the model quality with the highest value of  $Q_{\text{cmp}}$  (Figure 9i) being observed in the stability field of the inferred peak assemblage (see Figure 8c). This example shows that the choice of solid solution models can have a significant impact on  $Q_{\text{cmp}}$ . It is recommended to cross-check results of different databases especially when solid solutions are not reaching a  $Q_{\text{cmp}}$  value of 100% within the investigated  $P\text{--}T$  range, that is, the observed composition cannot be modelled within the uncertainty of the EPMA.

The maps of quality factors  $Q_{\text{cmp}}$  were recalculated with the database tc55 modified from Holland and Powell (1998) (Figure 9k–n). Solution models used in all calculations are those used in Pattison and Tinkham (2009). The maps of quality factor for each mineral show differences in the geometry of  $Q_{\text{cmp}}$  distribution and in the  $P\text{--}T$  position of the optimal conditions compared to those obtained with JUN92 database. These reflect the differences in the solid solution models. For instance, the melt model incorporated in tc55 (White, Powell, & Holland, 2007) impeded the stability of plagioclase and biotite at high temperatures and affects the modelled garnet composition (compare Figure 9f for JUN92 and 9l for tc55). However, optimal  $P\text{--}T$  conditions for  $Q_{\text{total}}$  (663°C and 0.69 GPa) differ only slightly from the results computed with JUN92 database (671°C and 0.64 GPa). These  $P\text{--}T$  conditions are interpreted as reflecting the equilibration conditions of the peak assemblage of this sample.

#### 4.6 | ITM using BINGO-ANTIDOTE—further investigations

A similar strategy can be applied to various domains within the mapped area. The mapped area was divided into a  $3 \times 3$  grid (Figure 10a) using *Recipe #11* and the evaluation criterion  $Q_{\text{total}2}$  assuming  $w_{\text{asm}} = 0.5$  and  $w_{\text{cmp}} = 0.5$  (software option, see Equation 7). In this example,  $Q_{\text{vol}}$  was not used ( $w_{\text{vol}} = 0$ ) to reduce the effects of changing modes on the total quality factor. A  $P\text{--}T$  trend is observed in the optimal

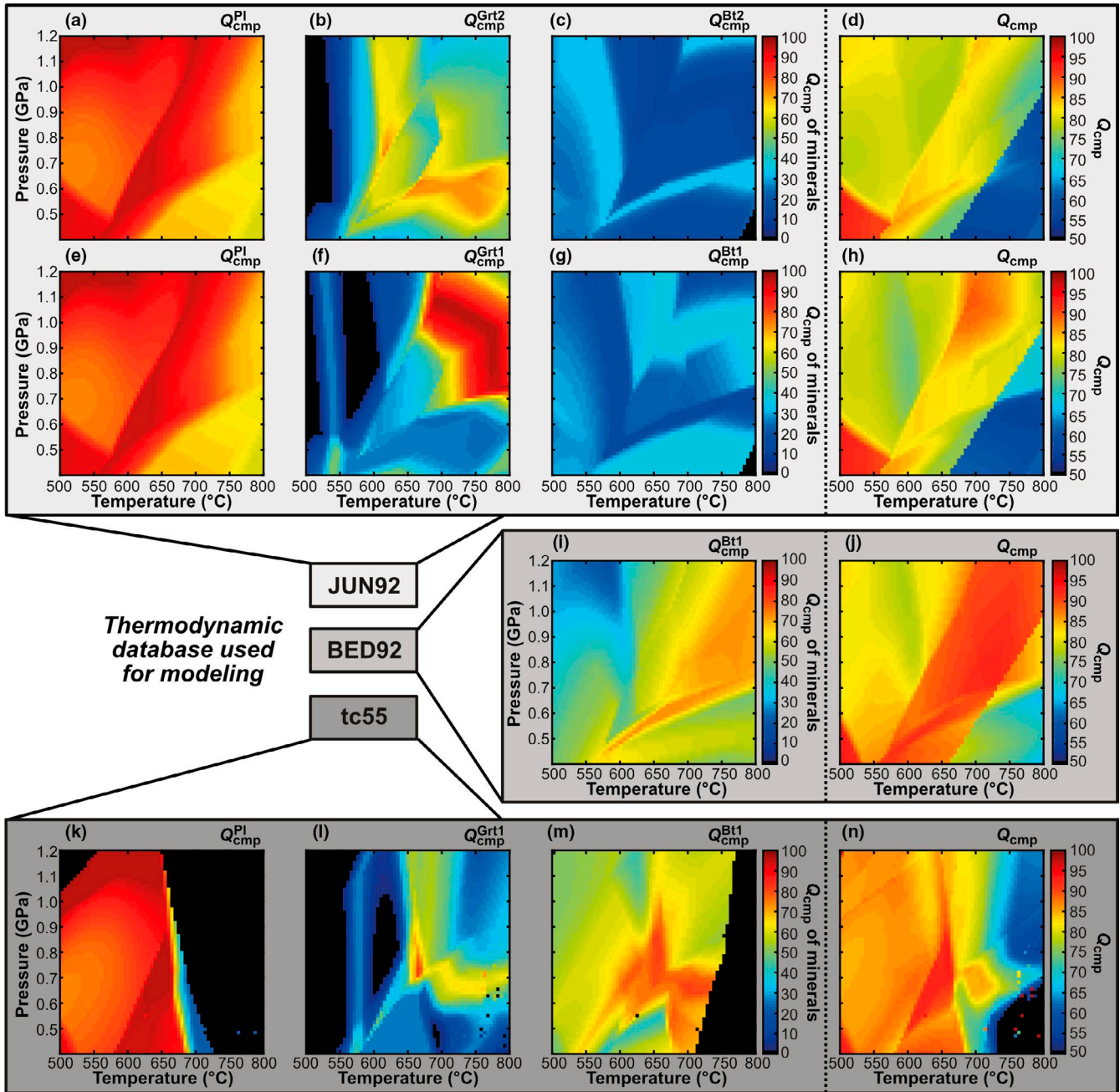


**FIGURE 9**  $P$ - $T$  maps of quality factor for  $Q_{\text{cmp}}$  of each solid solution involved in this example and generated based on different observed mineral compositions (e.g. core-rim) and thermodynamic databases. (a-d) Database JUN92 using garnet rim ( $\text{Grt}_2$ ) and adjacent biotite ( $\text{Bt}_2$ ), which were associated with the retrograde stage (see text). (e-h) Database JUN92 using garnet core ( $\text{Grt}_1$ ) and matrix biotite ( $\text{Bt}_1$ ), which are part of the inferred peak assemblage (see text). (e-h) Database JUN92 including an extended solution model for biotite (BED92, see text) and the compositions of matrix biotite ( $\text{Bt}_1$ ). In this model, the maps of  $Q_{\text{cmp}}$  for plagioclase and garnet are identical to (e) and (f). (k-n) Database tc55 including a melt model and using the compositions of garnet core ( $\text{Grt}_1$ ) and matrix biotite ( $\text{Bt}_1$ )

solution obtained for each position based on the database JUN92 (Figure 10b). For instance, optimal  $P$ - $T$  for 'window' w2 is 649°C and 0.59 GPa, whereas optimum for w6 is found at higher conditions of 695°C and 0.72 GPa. The solutions for w7-9 (670°C and 0.63 GPa) are in line with the  $P$ - $T$  conditions of  $\text{LBC}_1$  (Figure 10b). The domains with the lowest fraction of garnet yield lower  $P$ - $T$  conditions (e.g. window w2) than those with a high proportion of garnet (e.g. window

w6, see Figure 10c-e). This  $P$ - $T$  trend is only dictated by  $Q_{\text{cmp}}$ , since  $Q_{\text{asm}}$  is 100% for each model and  $Q_{\text{vol}}$  is not considered. The  $Q_{\text{cmp}}$  for garnet core and matrix biotite of w6 has the highest value ( $Q_{\text{cmp}}$  of 78% and 35% respectively), whereas w2 yields the lowest values. If composition of garnet rim and adjacent biotite (for the same determined  $P$ - $T$  conditions of each window) is used instead, the best value of  $Q_{\text{cmp}}$  of garnet rim composition is found for w9 (71%, whereas

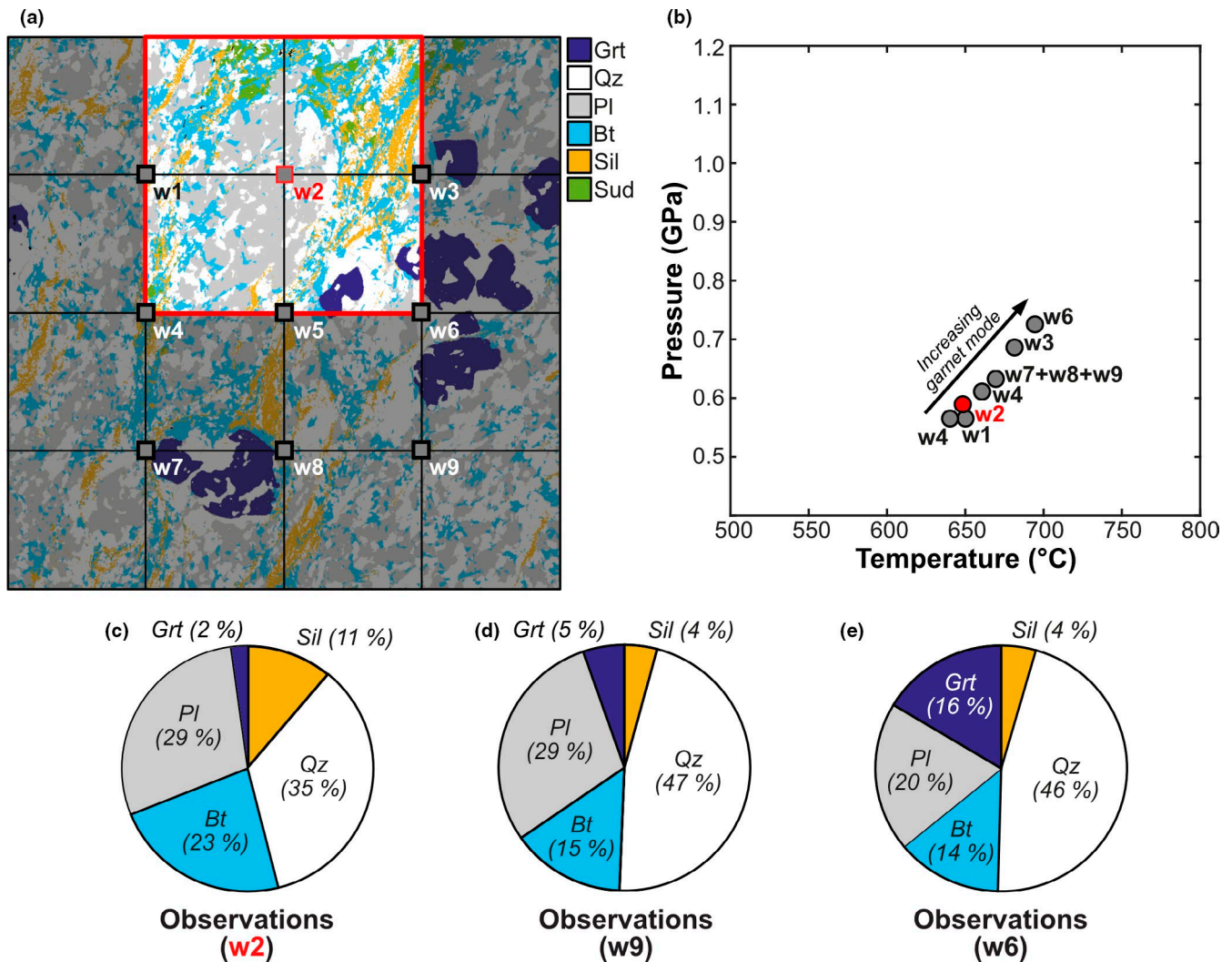


**FIGURE 10** Analysis of the local  $P$ - $T$  record via a scanning window and ITM. In this case, the objective function is defined by  $Q_{\text{total}2}$  assuming  $w_{\text{vol}}=0$  (see text). (a) Mineral distribution map subdivided into  $3 \times 3$  windows. (b) The ‘optimal’  $P$ - $T$  conditions calculated for the LBC of each window are shown in a  $P$ - $T$  diagram (b). Note that the results of window w7-9 (670°C and 0.63 GPa) are in line with the ‘optimal’  $P$ - $T$  conditions obtained for LBC<sub>1</sub> (compare with Figure 8). (c) Observed mineral modes for the models based on (c) w2; (d) w9 and (e) w6. Note that increasing fraction of garnet in the LBC is correlated with an increase in the apparent  $P$ - $T$  conditions. The window w2 in (a) and the corresponding result in (b) are highlighted in red

$Q_{\text{cmp}}$  of garnet core composition is 39%). The composition of adjacent biotite is best modelled using w2 ( $Q_{\text{cmp}}^{\text{Bt}} = 23\%$ ) corresponding to the garnet-absent area. It can also be noticed that w2 is the area containing (possible) former cordierite (now replaced by sudoite) and biotite with elevated  $X_{\text{Mg}}$  values (Figure 7), in line with lower re-equilibration temperatures. This  $P$ - $T$  trend mimics the  $P$ - $T$  maps of  $Q_{\text{cmp}}$  (see Figure 9). The metastable persistence of garnet core has a significant influence on the shape of this  $P$ - $T$  trend. Hence, it cannot be completely ruled out that the  $P$ - $T$  trend that closely moves along the staurolite to sillimanite stability field boundary represents the  $P$ - $T$  trajectory of this sample.

So far, the equilibrium conditions of staurolite, previously interpreted as retrograde, were not investigated because the grains in the mapped area were too small to be analysed with

a resolution of 20  $\mu\text{m}$ . A second map of a smaller domain located in an other area of the thin section was acquired at the Institute of Geosciences of the University of Kiel using a JEOL JXA-8900R superprobe with an accelerating voltage of 15 keV, specimen current of 100 nA, beam size of 1  $\mu\text{m}$  and a step size of 2  $\mu\text{m}$ . This domain was located far away from garnet to avoid re-equilibration of biotite by diffusion (see the garnet effect on spatial distribution of  $X_{\text{Mg}}$  of biotite in Figure 7e). The models presented in the following were computed using the database tc55 as this database provides the highest values of  $Q_{\text{cmp}}$  for staurolite and biotite (Figure 9). The optimization of  $Q_{\text{total}1}$  using *Recipe #1* resulted in two results (diamond and star in Figure 11a). Both solutions are not satisfactory, since one additional phase is predicted to be stable and not observed in this area (Figure 11b). At

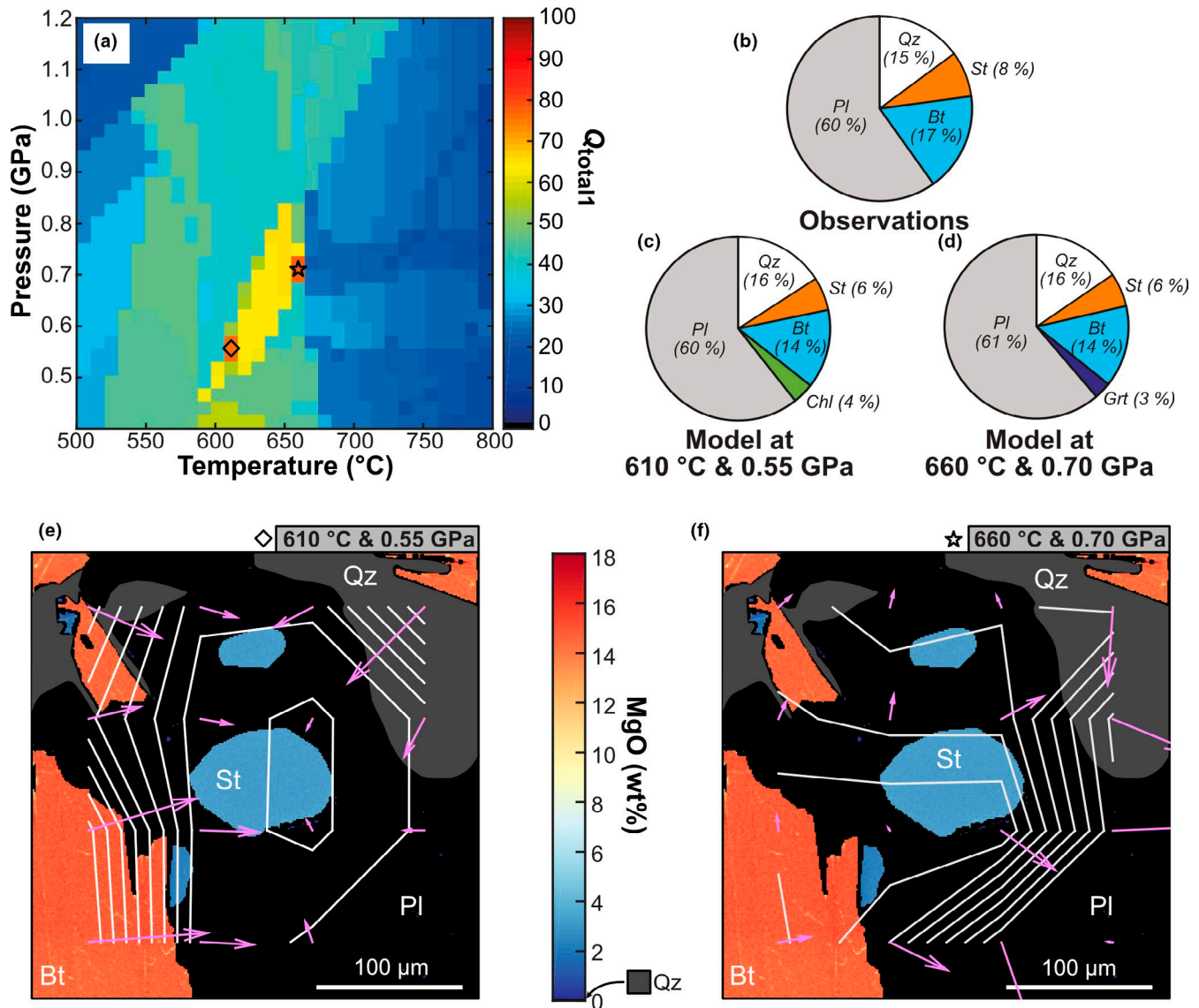


**FIGURE 11** Maps of chemical potential landscapes obtained for the second compositional map (see text) based on the database tc55 (see Appendix 1). Map of quality factor  $Q_{total1}$  with two statistically equivalent solutions (diamond and star symbols). (b) Mineral modes observed in the mapped area as obtained from the compositional maps. Modelled mineral modes at (c) 610°C, 0.55 GPa and (d) 660°C, 0.70 GPa. Maps of chemical potential landscape shown as quiver plots for  $\mu_{MgO}$  obtained at (e) 610°C, 0.55 GPa and (f) 660°C, 0.70 GPa. The contour levels are shown as white lines and correspond to isolines of chemical potential. The purple arrows show the gradient vectors; these are scaled to just not overlap

the lowest condition (610°C and 0.55 GPa), 4 vol.% chlorite is predicted to be stable, whereas 3 vol.% of garnet is predicted to be stable at the highest conditions (660°C and 0.7 GPa, see Figure 11c,d). As mentioned above, both phases were observed in the thin section. An interesting test is to determine at which conditions biotite and staurolite were in equilibrium. For both  $P$ - $T$  conditions, a chemical potential landscape map for  $\mu_{MgO}$  was computed (see Appendix 1). At 610°C and 0.55 GPa, the gradient in chemical potential is located between biotite and staurolite (Figure 10c). At 660°C and 0.7 GPa there is no steep gradient between staurolite and biotite and the compositions of the two minerals

are more compatible with chemical equilibrium (Figure 10c). Consequently, the model suggests that staurolite was part of the peak assemblage, that is, in chemical equilibrium with biotite, together with garnet (not on the plane of the compositional map, but in the near vicinity), at these conditions.

In summary, BINGO-ANTIDOTE helps to explore the equilibrium relationships in a sample at different spatial scales. Theoretical and natural examples will be discussed in the second paper of this series. For sample HAL104, the dominant phases re-equilibrated along the sillimanite to staurolite transition at ~660°C and 0.6–0.7 GPa. Later, biotite around garnet re-equilibrated locally with the garnet rims

at ~600°C and 0.55 GPa, occasionally with the presence of cordierite. Cordierite breakdown is predicted to take place at temperatures below 550°C, but the presence of sudoite suggests that this late replacement occurred at lower temperature conditions.

## 5 | DISCUSSION

Technical aspects related to the application of ITM using BINGO-ANTIDOTE are discussed below.

### 5.1 | Convergence problems and numerical instabilities

It is a well-known problem of optimization that a proper initial value and smooth gradients are critical for ensuring convergence to the global minimum. The objective function  $f$  is not smooth because of the effect of  $Q_{asm}$  on  $Q_{total}$  (e.g. Figure 8d). Any iterative optimization starting outside the optimal stability field is expected to fail and to converge to a local minimum. The size of the  $10 \times 10$  preliminary grid can be limited for large  $P$ - $T$  regions or in the presence of small stability fields. An increased resolution (e.g.  $100 \times 100$  or  $1,000 \times 1,000$ ) decreases the risks while increasing the computation time (by a factor of 100 and 10,000 respectively). It cannot be guaranteed with the optimization strategy employed in this study that a global minimum was found.

The optimization routine in ANTIDOTE assumes that the Gibbs free energy minimizer (here THERIAK) finds the stable mineral assemblage for  $X_{bulk}$ . In practice, this is not systematically the case as there are several reasons that can cause a minimization to fail (numerical instabilities, speciation calculations, components with trace concentrations, flat energy surfaces in non-ideal solution models). However, those have restricted effects on the optimization implemented in ANTIDOTE as the minimization failures systematically result in model outcomes with lower model quality factors. The minimization failures will be visible on the map of quality factor as they are on raw diagrams generated by THERIAK-DOMINO and PERPLE\_X. The number of failures can be reduced by using seeds (initial guesses) in THERIAK.

### 5.2 | Relative uncertainty and Monte Carlo simulations

BINGO-ANTIDOTE can be used for propagating relative uncertainty (e.g. the position of isopleths) resulting from the uncertainties of  $X_{bulk}$  through the forward model. Lanari and Engi (2017) showed that the differences in local bulk composition for a large-scale map have minor effects on the mineral

compositions and hence on related  $P$ - $T$  estimates. This is not the case for samples with more complex textures. The estimation of relative uncertainties in ANTIDOTE is based on the Monte Carlo technique, which is robust in multivariate statistics (systems with many degree of freedoms) and assumes that data are normally distributed. This assumption is to our knowledge reasonable within a given mineral assemblage (e.g. fig. 12 in Lanari & Engi, 2017) but is no longer valid if the assemblage changes.

### 5.3 | Textural and chemical equilibrium and user's assumptions

As revealed by the chemical potential landscape map, the a priori assumption made for the *classical sample preparation and analytical strategy* that staurolite was part of a retrograde assemblage was not valid. This example shows how assumptions drastically influence results, even if different methods (here isochemical phase diagram, BINGO, multi-equilibrium and garnet isopleths geothermobarometry) apparently agree (see Figures 5 and 6). Cross-checking of correlation of the *model quality factors* and especially the  $Q_{cmp}$  map of mineral groups may give hints about the validity of key assumptions concerning both the textural and chemical equilibrium. As postulated by Lanari and Engi (2017), a chemical domain is in chemical equilibrium at given  $P$ - $T$  conditions, if any smaller subdomain with the same mineral assemblage yields a similar  $P$ - $T$  estimate—a test that can be easily performed with ANTIDOTE (e.g. using the growing window recipe).

### 5.4 | Why THERIAK-DOMINO?

A Gibbs free energy minimizer is required for the optimization routine since the focus of Gibbs free energy minimizer is on the equilibrium assemblage rather than on the reactions of equilibrated phases. Software solutions based on linear equation solvers such as GIBBS or THERMOCALC are inappropriate. The two most used Gibbs free energy minimizers applied in metamorphic petrology are THERIAK and the MEEMUM routine of PERPLE\_X. The THERIAK routine was chosen here as the output format reduces the need for extra computations.

### 5.5 | Uncertainty of using different thermodynamic databases

BINGO-ANTIDOTE is built upon the THERIAK-DOMINO software package (de Capitani & Petrakakis, 2010) and can handle all thermodynamic databases available for THERIAK-DOMINO. Three main databases are distributed: (a) JUN92

(Berman, 1988 and subsequent updates), (b) tc55 (Holland & Powell, 1998 and subsequent updates) and (c) tc562c (Holland & Powell, 2011 and subsequent updates). These databases are still far from being perfect and covering all minerals and possible phase compositions (Forshaw, Waters, Pattison, Palin, & Gopon, 2019; Green et al., 2016; Santos, Moraes, & Szabó, 2019). Especially, the metamorphic modelling of rocks with a complex magmatic and polymetamorphic fluid–rock interaction history that features the formation of different generations of hydrous and extraordinary minerals (such as the Tudor Gabbro investigated by Duesterhoeft, Raase, & Gremler, 2017) is still an intractable problem. However, thermodynamic databases comprise data for a large amount of minerals and are a powerful tool to understand the nature of metamorphic processes. Theoretically, all thermodynamic databases should result in similar outcome because all are based on the principle of Gibbs energy and they are calibrated on a similar data set of experimental data. Nevertheless, discrepancies exist due to the application of different equation of state (Duesterhoeft, 2016; Freund & Ingalls, 1989), different solid solution models, and different number of implemented mineral phases (Lanari & Duesterhoeft, 2019). Consequently, the user should know the strengths and weaknesses of the applied database or alternatively compare the outcome applying different databases. The BINGO-ANTIDOTE strategy is quick and relatively objective, allowing the user to quantify the differences between thermodynamic databases within a couple of minutes.

## 6 | CONCLUSION

This study presents the first hybrid approach and the software solution BINGO-ANTIDOTE combining the strengths of forward GEM models with the intuitive output of inverse models. The scoring strategy of BINGO and a large variety of optimization routines in ANTIDOTE permit (a) to explore equilibrium textures at the thin section scale and the determination of associated  $P$ – $T$  conditions, (b) the estimation of uncertainties. The models (c) can be restricted to well-equilibrated mineral phases, excluding metastable phases (e.g. associated ores, phosphates or secondary minerals such as chlorites or clays) from the reactive bulk composition and (d) provide a quick and objective comparison between different thermodynamic databases.

BINGO-ANTIDOTE can be used within XMAPTOOLS or as a standalone version. In the standalone version, the macroscopic observations (i.e. mineral names and proportions) are converted by ANTIDOTE to a readable BINGO input. The application of BINGO-ANTIDOTE opens up thermodynamics to students and people with only a basic knowledge of phase diagrams and thermodynamic modelling techniques.

## SOFTWARE AVAILABILITY

BINGO-ANTIDOTE software is implemented in the add-on XTHERMOTOOLS that is compatible with XMAPTOOLS 3.4 and more recent versions (<https://www.xmaptools.com>). A copy of the standalone version can be obtained via the Github repository <https://github.com/lanari/bingo-antidote>

## ACKNOWLEDGEMENTS

The research was supported by the German Research Foundation (DFG) research grant DU1603/1-1. The development of BINGO-ANTIDOTE has benefited from discussions with Rob Berman, Romain Bousquet, Marco Burn, Christian de Capitani, Martin Engi, Joerg Hermann, Amaury Pourteau, Nicolas Riel, Daniela Rubatto, Mahyra Tedeschi, Alice Vho and Thereza Yogi. We are very grateful to Evangelos Moulas and Katy Evans for their careful and meticulous reading of the paper.

## ORCID

Erik Duesterhoeft  <https://orcid.org/0000-0002-4753-905X>

Pierre Lanari  <https://orcid.org/0000-0001-8303-0771>

## REFERENCES

- Anovitz, L., & Essene, E. (1990). Thermobarometry and pressure-temperature paths in the Grenville Province of Ontario. *Journal of Petrology*, 31, 197–241. <https://doi.org/10.1093/ptrology/31.1.197>
- Berman, R. G. (1988). Internally-consistent thermodynamic data for minerals in the system Na<sub>2</sub>O-K<sub>2</sub>O-CaO-MgO-FeO-Fe<sub>2</sub>O<sub>3</sub>-Al<sub>2</sub>O<sub>3</sub>-SiO<sub>2</sub>-TiO<sub>2</sub>-H<sub>2</sub>O-CO<sub>2</sub>. *Journal of Petrology*, 29(2), 445–552. <https://doi.org/10.1093/ptrology/29.2.445>
- Berman, R. G. (2007). WinTWQ (version 2.3) a software package for performing internally-consistent thermobarometric calculations. Geological Survey of Canada, Open File, 5462, 41.
- Berman, R. G., Aranovich, L. Y., Rancourt, D. G., & Mercier, P. H. J. (2007). Reversed phase equilibrium constraints on the stability of Mg-Fe-Al biotite. *American Mineralogist*, 92(1), 139–150. <https://doi.org/10.2138/am.2007.2051>
- Brown, T. H., & Skinner, B. J. (1974). Theoretical prediction of equilibrium phase assemblages in multicomponent systems. *American Journal of Science*, 274(9), 961–986. <https://doi.org/10.2475/ajs.274.9.961>
- Carlson, W. D., Pattison, D. R. M., & Caddick, M. J. (2015). Beyond the equilibrium paradigm: How consideration of kinetics enhances metamorphic interpretation. *American Mineralogist*, 100(8–9), 1659–1667. <https://doi.org/10.2138/am-2015-5097>
- Clarke, G. L., Daczko, N. R., & Nockolds, C. (2001). A method for applying matrix corrections to X-ray intensity maps using the Bence-Albee algorithm and Matlab. *Journal of Metamorphic Geology*, 19(6), 635–644. <https://doi.org/10.1046/j.0263-4929.2001.00336.x>
- Connolly, J. A. D. (1990). Multivariable phase diagrams: An algorithm based on generalized thermodynamics. *American Journal of Science*, 290, 666–718. <https://doi.org/10.2475/ajs.290.6.666>

- Connolly, J. A. D. (2005). Computation of phase equilibria by linear programming: A tool for geodynamic modeling and its application to subduction zone decarbonation. *Earth and Planetary Science Letters*, 236(1–2), 524–541. <https://doi.org/10.1016/j.epsl.2005.04.033>
- Connolly, J. A. D. (2005). Computation of phase equilibria by linear programming: A tool for geodynamic modeling and its application to subduction zone decarbonation. *Earth and Planetary Science Letters*, 236(1–2), 524–541. <https://doi.org/10.1016/j.epsl.2005.04.033>
- Connolly, J. A. D. (2009). The geodynamic equation of state: What and how. *Geochemistry, Geophysics, Geosystems*, 10(10), 1–19. <https://doi.org/10.1029/2009GC002540>
- Connolly, J. A. D., & Kerrick, D. M. (1987). An algorithm and computer program for calculating composition phase diagrams. *CALPHAD*, 11(1), 1–55. [https://doi.org/10.1016/0364-5916\(87\)90018-6](https://doi.org/10.1016/0364-5916(87)90018-6)
- De Andrade, V., Vidal, O., Lewin, E., O'Brien, P., & Agard, P. (2006). Quantification of electron microprobe compositional maps of rock thin sections: An optimized method and examples. *Journal of Metamorphic Geology*, 24(7), 655–668. <https://doi.org/10.1111/j.1525-1314.2006.00660.x>
- de Capitani, C., & Brown, T. H. (1987). The computation of chemical equilibrium in complex systems containing non-ideal solutions. *Geochimica et Cosmochimica Acta*, 51(10), 2639–2652. [https://doi.org/10.1016/0016-7037\(87\)90145-1](https://doi.org/10.1016/0016-7037(87)90145-1)
- de Capitani, C., & Petrakakis, K. (2010). The computation of equilibrium assemblage diagrams with Theriak/Domino software. *American Mineralogist*, 95(7), 1006–1016. <https://doi.org/10.2138/am.2010.3354>
- Duesterhoeft, E. (2016). A volume equation of state that extends thermodynamic datasets, using the Bridgman power series, to very high pressures (20 GPa). *American Journal of Science*, 316(6), 578–589. <https://doi.org/10.2475/06.2016.03>
- Duesterhoeft, E. (2017). BED92.v1 – Theriak-Domino database. ResearchGate. <http://doi.org/10.13140/RG.2.2.10285.69609>
- Duesterhoeft, E., & de Capitani, C. (2013). Theriak\_D: An add-on to implement equilibrium computations in geodynamic models. *Geochemistry, Geophysics, Geosystems*, 14(11), 4962–4967. <https://doi.org/10.1002/ggge.20286>
- Duesterhoeft, E., Raase, P., & Gremler, P. (2017). A new occurrence of extremely rare Ferro-Chloro-Pargasite in Tudor, Ontario. *International Journal of Earth Sciences*, 106(8), 2815–2816. <https://doi.org/10.1007/s00531-017-1492-7>
- Dunn, S. R., Markley, M. J., Kotikian, M., Achenbach, K., Montanye, B., & Peck, W. H. (2019). Geothermometry of the Western Half of the Central Metasedimentary Belt, Grenville Province, Ontario, and its Implications. *American Mineralogist*, 104, 791–809. <https://doi.org/10.2138/am-2019-6757>
- Forshaw, J. B., Waters, D. J., Pattison, D. R. M., Palin, R. M., & Gopon, P. (2019). A comparison of observed and thermodynamically predicted phase equilibria and mineral compositions in mafic granulites. *Journal of Metamorphic Geology*, 37(2), 153–179. <https://doi.org/10.1111/jmg.12454>
- Freund, J., & Ingalls, R. (1989). Inverted isothermal equations of state and determination of B<sub>0</sub>, B'<sub>0</sub> and B''<sub>0</sub>. *Journal of Physics and Chemistry of Solids*, 50(3), 263–268. [https://doi.org/10.1016/0022-3697\(89\)90486-1](https://doi.org/10.1016/0022-3697(89)90486-1)
- Green, E. C. R., White, R. W., Diener, J. F. A., Powell, R., Holland, T. J. B., & Palin, R. M. (2016). Activity–composition relations for the calculation of partial melting equilibria in metabasic rocks. *Journal of Metamorphic Geology*, 34(9), 845–869. <https://doi.org/10.1111/jmg.12211>
- Guevara, V. E., & Caddick, M. J. (2016). Shooting at a moving target: Phase equilibria modelling of high-temperature metamorphism. *Journal of Metamorphic Geology*, 34(3), 209–235. <https://doi.org/10.1111/jmg.12179>
- Hanmer, S. (1988). Ductile thrusting at mid-crustal level, southwestern Grenville Province. *Canadian Journal of Earth Sciences*, 25, 1049–1059. <https://doi.org/10.1139/e88-102>
- Hanmer, S. (1989). *Geology, western part of the central metasedimentary belt boundary zone*. Ontario: Grenville Province. Geological Survey of Canada: Ottawa, ON, Canada. Map 1688A, scale 1:50 000.
- Henry, D. J., Guidotti, C. V., & Thomson, J. A. (2005). The Ti-saturation surface for low-to-medium pressure metapelitic biotites: Implications for geothermometry and Ti-substitution mechanisms. *American Mineralogist*, 90(2-3), 316–328. <https://doi.org/10.2138/am.2005.1498>
- Holland, T. J. B., & Powell, R. (1998). An internally consistent thermodynamic data set for phases of petrological interest. *Journal of Metamorphic Geology*, 16(3), 309–343. <https://doi.org/10.1111/j.1525-1314.1998.00140.x>
- Holland, T. J. B., & Powell, R. (2011). An improved and extended internally consistent thermodynamic dataset for phases of petrological interest, involving a new equation of state for solids. *Journal of Metamorphic Geology*, 29(3), 333–383. <https://doi.org/10.1111/j.1525-1314.2010.00923.x>
- Kohn, M. J., & Spear, F. (2000). Retrograde net transfer reaction insurance for pressure-temperature estimates. *Geology*, 28(12), 1127–1130. [https://doi.org/10.1130/0091-7613\(2000\)28<1127:RNTRIF>2.0.CO;2](https://doi.org/10.1130/0091-7613(2000)28<1127:RNTRIF>2.0.CO;2)
- Lanari, P., & Duesterhoeft, E. (2019). Modeling metamorphic rocks using equilibrium thermodynamics and internally consistent databases: Past achievements, problems and perspectives. *Journal of Petrology*, 60(1), 19–56. <https://doi.org/10.1093/petrology/egy105>
- Lanari, P., & Engi, M. (2017). Local bulk composition effects on metamorphic mineral assemblages. *Reviews in Mineralogy and Geochemistry*, 83, 55–102. <https://doi.org/10.2138/rmg.2017.83.3>
- Lanari, P., Giuntoli, F., Loury, C., Burn, M., & Engi, M. (2017). An inverse modeling approach to obtain P-T conditions of metamorphic stages involving garnet growth and resorption. *European Journal of Mineralogy*, 29, 181–199. <https://doi.org/10.1127/ejm/2016/0029-2597>
- Lanari, P., Vho, A., Bovay, T., Airaghi, L., & Centrella, S. (2019). Quantitative compositional mapping of mineral phases by electron probe micro-analyser. *Geological Society Special Publication*, 478(1), 39–63. <https://doi.org/10.1144/SP478.4>
- Lanari, P., Vidal, O., De Andrade, V., Dubacq, B., Lewin, E., Grosch, E. G., & Schwartz, S. (2014). XMapTools: A MATLAB®-based program for electron microprobe X-ray image processing and geothermobarometry. *Computers & Geosciences*, 62, 227–240. <https://doi.org/10.1016/j.cageo.2013.08.010>
- Lanari, P., Wagner, T., & Vidal, O. (2014). A thermodynamic model for di-trioctahedral chlorite from experimental and natural data in the system MgO–FeO–Al<sub>2</sub>O<sub>3</sub>–SiO<sub>2</sub>–H<sub>2</sub>O: applications to P-T sections and geothermometry. *Contributions to Mineralogy and Petrology*, 167–968. <https://doi.org/10.1007/s00410-014-0968-8>

- Markley, M. J., Dunn, S. R., Jercinovic, M. J., Peck, W. H., & Williams, M. L. (2018). Monazite U–Th–Pb geochronology of the Central Metasedimentary Belt Boundary Zone (CMBbz), Grenville Province, Ontario Canada. *Canadian Journal of Earth Sciences*, 55(9), 1063–1078. <https://doi.org/10.1139/cjes-2018-0039>
- McEachern, S. J., & van Breemen, O. (1993). Age of deformation within the Central Metasedimentary Belt boundary thrust zone, southwest Grenville Orogen: Constraints on the collision of the Mid-Proterozoic Elzevir terrane. *Canadian Journal of Earth Sciences*, 30, 1155–1165. <https://doi.org/10.1139/e93-098>
- Nelder, J. A., & Mead, R. (1965). A simplex method for function minimization. *The Computer Journal*, 7(4), 308–313. <https://doi.org/10.1093/comjnl/7.4.308>
- Palin, R. M., Weller, O. M., Waters, D. J., & Dyck, B. (2016). Quantifying geological uncertainty in metamorphic phase equilibria modelling: A Monte Carlo assessment and implications for tectonic interpretations. *Geoscience Frontiers*, 7(4), 591–607. <https://doi.org/10.1016/j.gsf.2015.08.005>
- Pattison, D. R. M., & Spear, F. S. (2018). Kinetic control of staurolite–Al<sub>2</sub>SiO<sub>5</sub> mineral assemblages: Implications for Barrovian and Buchan metamorphism. *Journal of Metamorphic Geology*, 36(6), 667–690. <https://doi.org/10.1111/jmg.12302>
- Pattison, D. R. M., & Tinkham, D. K. (2009). Interplay between equilibrium and kinetics in prograde metamorphism of pelites: An example from the Nelson aureole, British Columbia. *Journal of Metamorphic Geology*, 27(4), 249–279. <https://doi.org/10.1111/j.1525-1314.2009.00816.x>
- Powell, R., & Holland, T. J. B. (2008). On thermobarometry. *Journal of Metamorphic Geology*, 26(2), 155–179. <https://doi.org/10.1111/j.1525-1314.2007.00756.x>
- Powell, R., Holland, T., & Worley, B. (1998). Calculating phase diagrams involving solid solutions via non-linear equations, with examples using THERMOCALC. *Journal of Metamorphic Geology*, 16, 577–588. <https://doi.org/10.1111/j.1525-1314.1998.00157.x>
- Santos, C. A., Moraes, R., & Szabó, G. A. J. (2019). A comparison between phase diagram modelling of metamorphic rocks and experimental and independent thermobarometric data. *Lithos*, 340–341, 108–123. <https://doi.org/10.1016/j.lithos.2019.04.024>
- Shrestha, S., Larson, K. P., Duesterhoeft, E., Soret, M., & Cottle, J. M. (2019). Thermodynamic modelling of phosphate minerals and its implications for the development of P–T–t histories: A case study in garnet – monazite bearing metapelites. *Lithos*, 334–335, 141–160. <https://doi.org/10.1016/j.lithos.2019.03.021>
- Spear, F. S., Pattison, D. R. M., & Cheney, J. T. (2016). The metamorphism of metamorphic petrology. *Geological Society of America Special Paper*, 523(02), 31–74. [https://doi.org/10.1130/2016.2523\(02\)](https://doi.org/10.1130/2016.2523(02))
- Spear, F. S., & Pyle, J. M. (2010). Theoretical modeling of monazite growth in a low-Ca metapelite. *Chemical Geology*, 273(1–2), 111–119. <https://doi.org/10.1016/j.chemgeo.2010.02.016>
- Stüwe, K. (1997). Effective bulk composition changes due to cooling: A model predicting complexities in retrograde reaction textures. *Contributions to Mineralogy and Petrology*, 129(1), 43–52. <https://doi.org/10.1007/s004100050322>
- Tajčmanová, L., Konopásek, J., & Schulmann, K. (2006). Thermal evolution of the orogenic lower crust during exhumation within a thickened Moldanubian root of the Variscan belt of Central Europe. *Journal of Metamorphic Geology*, 24(2), 119–134. <https://doi.org/10.1111/j.1525-1314.2006.00629.x>
- Waters, D. J., & Lovegrove, D. P. (2002). Assessing the extent of disequilibrium and overstepping of prograde metamorphic reactions in metapelites from the Bushveld Complex aureole, South Africa. *Journal of Metamorphic Geology*, 20(1), 135–149. <https://doi.org/10.1046/j.0263-4929.2001.00350.x>
- White, R. W., Powell, R., & Holland, T. J. B. (2007). Progress relating to calculation of partial melting equilibria for metapelites. *Journal of Metamorphic Geology*, 25(5), 511–527. <https://doi.org/10.1111/j.1525-1314.2007.00711.x>
- White, R. W., Powell, R., Holland, T. J. B., Johnson, T. E., & Green, E. C. R. (2014). New mineral activity–composition relations for thermodynamic calculations in metapelitic systems. *Journal of Metamorphic Geology*, 32(3), 261–286. <https://doi.org/10.1111/jmg.12071>
- Yakymchuk, C. (2017). Applying phase equilibria modelling to metamorphic and geological processes: Recent developments and future potential. *Geoscience Canada*, 44(1), 27. <https://doi.org/10.12789/geocanj.2017.44.114>

**How to cite this article:** Duesterhoeft E, Lanari P. Iterative thermodynamic modelling—Part I: A theoretical scoring technique and a computer program (BINGO-ANTIDOTE). *J Metamorph Geol*. 2020;38:527–551. <https://doi.org/10.1111/jmg.12538>

## APPENDIX 1

The description of ANTIDOTE's Recipe #13 that generates maps of chemical potential gradient landscapes calculated at fixed  $P$ – $T$  conditions is outlined here. The application example used (Figure A1) is presented in Figure 11e of the paper.

### Algorithm for chemical potential mapping

The mapped area is divided into a set of smaller domains from which local bulk compositions (LBCs) can be extracted. The chemical potentials of the oxide components are calculated for each LBC based on the stable mineral assemblage obtained via GEM at fixed  $P$ – $T$  conditions assuming chemical equilibrium for the local bulk composition. A contour map is displayed using isolines of chemical potential (e.g. Figure 11e).

For a compositional map having  $y$  rows and  $x$  columns, the centre position of a rectangular window with a length  $l$  and width  $w$  is moved along a regular two-dimensional grid having a spacing of  $dX$  and  $dY$ . The values of  $l$  and  $dX$  are expressed in number of pixels (from the compositional maps) and are set by the user (software option). The  $l/w$  ratio of the rectangular window is equal to  $x/y$  and the window is moved

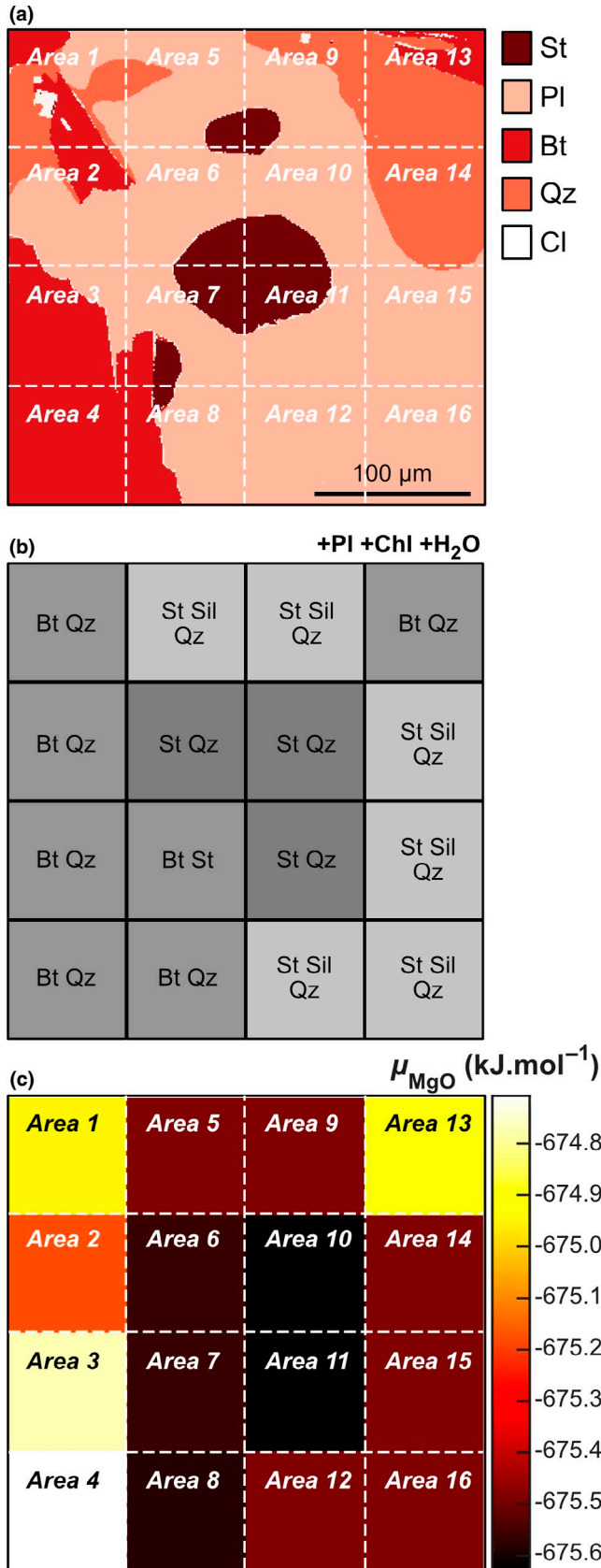


**FIGURE A1** Generation of chemical potential landscape maps. (a) Mineral distribution map for the mapped area and windows used to calculate the LBCs. Abbreviation: Cl, clay. (b) Mineral assemblage predicted to be stable at 610°C and 0.55 GPa in each window. (c) Map of chemical potential showing the value of  $\mu_{\text{MgO}}$  calculated by GEM for each window

along a regular grid ( $dY = dX$ ). The  $X_i$  values of the grid in the interval.

$$\left[ \frac{dX-1}{2}, \frac{dX-1}{2} + dX, \frac{dX-1}{2} + 2 \cdot dX, \dots, \frac{dX-1}{2} + n \cdot dX \right].$$

are generated using the numeric vector:

$$X_i = \left[ \frac{dX-1}{2} : dX : x - \frac{dX-1}{2} \right].$$

Note that if  $x - \frac{dX-1}{2}$  is not an increment of  $dX$ , then the last value of the vector stops before. If  $dX < l$ , two successive windows have an horizontal overlapping of  $l - dX$ . If  $dX > l$ , a rectangular area with a length of  $dX - l$  is not sampled between two successive windows. Similarly, the  $Y_j$  values are generated using the numeric vector:

$$Y_j = \left[ \frac{dY-1}{2} : dY : y - \frac{dY-1}{2} \right].$$

A local bulk composition LBC is obtained by integrating the composition of the pixels (corrected for density) in each window and used as input in the GEM-based model. The chemical potential of each oxide component is calculated by THERIAK provided that this chemical potential is buffered for the modelled mineral assemblage.

**Proof of concept**

The chemical potentials were calculated using THERIAK at 600°C and 0.7 GPa in the system SiO<sub>2</sub>-Al<sub>2</sub>O<sub>3</sub>-FeO-MgO-H<sub>2</sub>O for the LBCs of five virtual windows involving various phase proportions (see the table below). Water was assumed to be in excess in all simulations. Reference mineral compositions of chlorite, staurolite, kyanite and quartz were extracted from a preliminary simulation conducted at the same *P-T* conditions using an arbitrary bulk composition (0.5 mole of Si, 0.25 mole of Al, 0.04 mole of Fe, 0.1 mole of Mg and 1 mole of H) and they are used in the following to calculate the LBCs. The results are:

	Window 1	Window 2	Window 3	Window 4	Window 5
	LBC-1	LBC-2	LBC-3	LBC-4	LBC-5
	Chl-absent		Ky-absent		St-absent
Modelled mineral modes (vol.%) <sup>a</sup>					
St	55.30	48.85	40.82	14.64	0.000
Chl	0.000	11.53	38.39	45.91	53.80
Qz	28.17	24.92	20.79	24.87	29.13
Ky	16.53	14.71	0.000	14.58	17.07
Chemical potential of components (kJ/mol) <sup>a</sup>					
$\mu_{\text{MgO}}$	-672.358	-672.358	-672.358	-672.358	-672.358
$\mu_{\text{H}_2\text{O}}$	-357.116	-357.116	-357.116	-357.116	-357.116
$\mu_{\text{FeO}}$	-352.121	-352.121	-352.121	-352.121	-352.121
$\mu_{\text{SiO}_2}$	-951.032	-951.032	-951.032	-951.032	-951.032
$\mu_{\text{Al}_2\text{O}_3}$	-17,39.75	-1,739.75	-1,739.75	-1,739.75	-1,739.75

<sup>a</sup> At 600°C 0.7 GPa.

As the same mineral compositions are used in each ‘window’, this model simulates a scenario in which no compositional zoning is observed in the mapped area and the value of  $Q_{\text{total}}$  is systematically 100%. In this case, there is no difference in chemical potential observed through the area even though the mineral modes are changing and chlorite, kyanite and staurolite are absent in at least one window.

In a second example, chlorite was replaced by garnet, which is not predicted to be stable at 600°C and 0.7 GPa in this chemical system. It simulates the investigation of minerals that did not form in equilibrium and did not re-equilibrate. The results between the garnet-absent and the kyanite-absent areas (for windows 1, 2 and 3) are:

	Window 1	Window 2	Window 3
	LBC-1	LBC-6	LBC-7
	Grt-absent		Ky-absent

Modelled mineral modes (vol.%)<sup>a</sup>

St	55.30	69.57	40.45
Chl	0.000	0.000	14.44
Qz	28.17	29.80	36.40
Ky	16.53	0.632	0.000
Grt	0.000	0.000	8.721

Chemical potential of components (kJ/mol)<sup>a</sup>

$\mu_{\text{MgO}}$	-672.358	-672.588	-674.013
$\mu_{\text{H}_2\text{O}}$	-357.116	-357.116	-357.116
$-Q_{\text{total}}$	-352.121	-351.991	-346.993
$\mu_{\text{SiO}_2}$	-951.032	-951.032	-951.032
$\mu_{\text{Al}_2\text{O}_3}$	-1739.75	-1739.75	-1741.16

<sup>a</sup> At 600°C 0.7 GPa.

In this case, chemical potential gradients in  $\mu_{\text{MgO}}$  (-1.655 kJ/mol),  $\mu_{\text{FeO}}$  (+5.128 kJ/mol) and  $\mu_{\text{Al}_2\text{O}_3}$  (-1.410 kJ/mol) are obtained between window 1 (garnet absent) and window 3 (garnet present and kyanite absent). The direction of the gradient indicates that the diffusion of MgO and  $\text{Al}_2\text{O}_3$  from window 1 to window 3 and the diffusion of FeO from window 3 to window 1 would be required to flatten this gradient and to converge towards chemical equilibrium at these conditions. This reaction would involve the replacement of garnet by chlorite. Note that there are no gradients in  $\mu_{\text{SiO}_2}$  and  $\mu_{\text{H}_2\text{O}}$  as both quartz and  $\text{H}_2\text{O}$  fluid are predicted to be stable throughout.

These two examples demonstrate that the presence of chemical potential gradients in a given microstructure can be used to infer minerals that are not compatible with chemical equilibrium at the  $P$ - $T$  conditions of interest (e.g. garnet in scenario 2). However, the absolute values of chemical potential obtained using this technique can only be used as qualitative indicators as they are obtained via GEM assuming chemical equilibrium, which was obviously not the case if  $Q_{\text{total}}$  is not 100%. In the second example, chemical equilibrium was not achieved in windows 2 and 3 (with garnet) which were not re-equilibrated at 600°C and 0.7 GPa for their local bulk compositions LBC-6 and LBC-7.

### Application to compositional maps

A small compositional map—of 300 × 300 pixels with a pixel size of 2 μm—containing plagioclase, staurolite, biotite and quartz is used (Figure A1a). The mapped area was divided into 16 squared windows ( $l=w$ ) having a length of 75 pixels (Areas 1–16 in Figure A1c). The grid spacing was set to 75 pixels in order to sample the entire area and avoid overlapping. A total of 16 LBCs were obtained:

	LBC-1	LBC-2	LBC-3	LBC-4	LBC-5	LBC-6	LBC-7	LBC-8
Al <sub>2</sub> O <sub>3</sub>	12.06	17.76	17.99	17.36	22.41	26.86	31.87	20.40
CAO	0.302	0.655	0.198	0.016	0.873	0.883	0.625	0.673
FEO	5.352	3.911	12.71	15.35	1.427	2.823	6.452	5.547
K <sub>2</sub> O	3.267	2.424	7.688	9.551	0.071	0.087	0.896	3.241
MGO	4.981	3.686	12.14	14.63	0.312	0.644	2.447	4.997
NA <sub>2</sub> O	3.242	7.091	2.073	0.207	9.177	8.732	6.06	6.892
SIO <sub>2</sub>	68.10	62.44	41.31	35.69	65.358	59.30	49.89	55.53

The mineral assemblage predicted to be stable at 610°C and 0.55 GPa in each window is shown in Figure A1b and the corresponding map of  $\mu_{\text{MgO}}$  in Figure A1c. The contour map shown in Figure 11e was derived from Figure A1c. The main gradient in  $\mu_{\text{MgO}}$  is observed between the two

assemblages biotite–quartz–plagioclase–chlorite–H<sub>2</sub>O and staurolite–quartz–plagioclase–chlorite–H<sub>2</sub>O suggesting that diffusion of MgO downward the chemical potential gradient would be required to reach chemical equilibrium at these  $P$ – $T$  conditions.